Geophysical Journal International

Geophys. J. Int. (2025) **243,** 1–19
Advance Access publication 2025 July 24
Research Paper

https://doi.org/10.1093/gji/ggaf282

Ambient noise crustal imaging of a heterogeneous rift linkage zone: Turkana Depression, East Africa

M. Musila [1], F. Civilini,[2] C. J. Ebinger,[1] I. D. Bastow,[3] R. Kounoudis,[4] C.S. Ogden [4] and N. Mariita[5]

[1] *Department of Earth and Environmental Sciences, Tulane University, New Orleans, LA 70118, USA. E-mail: mmusila@tulane.edu*
[2] *NASA Goddard Space Flight Center, Greenbelt, MD 20771, USA. E-mail: francesco.civilini@nasa.gov*
[3] *Department of Earth Science and Engineering, Imperial College, London SW7 2AZ, UK. E-mail: i.bastow@imperial.ac.uk*
[4] *Department of Earth Sciences, University of Oxford, Oxford, OX1 3AN, UK. E-mail: rita.kounoudis@earth.ox.ac.uk*
[5] *Geothermal Energy Training and Research Institute, Dedan Kimathi University of Technology, Nyeri, 10100, Kenya. E-mail: nicholas.mariita@dkut.ac.ke*

Accepted 2025 July 21. Received 2025 June 9; in original form 2025 March 11

SUMMARY

The role of pre-existing lithospheric heterogeneities in rifting processes remains unclear. The Eastern and Main Ethiopian rifts lie within the same geodynamic province and are kinematically connected through the Turkana Depression, but they transect heterogeneous lithosphere: Pan-African accreted terranes, failed Mesozoic-Paleogene rift systems, zones of Eocene–Oligocene flood magmatism. Rifting in these pre-extension heterogeneities offers the opportunity to evaluate their relative importance in Oligo-Miocene to Recent stretching and magmatism. We use 3-D Rayleigh shear-wave speed (Vs) models inverted from ambient noise signals recorded on a temporary seismic network to image heterogeneities in lithospheric structure, and to evaluate their influence on syn-rift faulting and magmatism. Crustal feeder zones for Eocene–Oligocene flood magmatism in southwestern Ethiopia are marked by $\leq$50 km-wide, 10–15 km-thick mid-lower crustal fast wave speed (Vs $\geq$ 3.8 km s^{-1}) anomalies that are localized rather than widespread. Evidence for active magma intrusions only occurs beneath aligned chains of Quaternary eruptive centres in Lake Turkana and $\leq$1 Ma shield volcanoes east of the Turkana rift having localized low Vs ($\leq$3.4 km s^{-1}) at 0–20 km depth. Evidence for widespread lower crustal intrusions, however, is lacking. Pan-African oceanic accreted terranes in southern Ethiopia have high Vs anomalies of 3.6 km s^{-1} throughout the crust and overlay previously imaged high-wave speed lithospheric mantle that has been interpreted as cold and strong Proterozoic accreted terrane. The integrated strength of this lithospheric-scale pre-existing mechanical heterogeneity resisted Oligocene–Miocene stretching and subsequently contributed to the unusual breadth of this East African rift sector lying north of the Turkana Depression.

Key words: Crustal imaging; Seismic tomography; Continental tectonics: extensional; Crustal structure; Large igneous provinces.

1 INTRODUCTION

Data and models have shown that progressive thinning and weakening of strong, thick lithosphere as rifting progresses to incipient sea floor spreading is accommodated through a combination of (1) mechanical plate stretching that thins the crust and the mantle lithosphere; (2) conductive heating from passively or dynamically upwelling asthenosphere; (3) advective thinning at the base of the plate; and (4) heating and extension achieved by magma intrusions sourced from adiabatic decompression melting of the asthenosphere with melt and volatile contributions from the lithosphere (e.g. Chin 2018; Ebinger 2021; Brune *et al.* 2023; Ozaydin *et al.* 2024). Yet, these conceptual models of continental rifting, constrained by geoscientific studies, do not account for plate heterogeneity associated with pre-existing structures and strength variations such as exotic terranes, pre-existing rift zones and pre-rift flood magmatism that may affect the continental rift's breadth, orientation and style of strain localization (e.g. Guerri *et al.* 2015; Wenker & Beaumont 2018; Neves et al. 2021; Musila *et al.* 2023). New and existing seismic data from the actively deforming Turkana Depression region of East Africa offer the opportunity to evaluate lateral heterogeneities and their spatial relationship to faults, pre-rift crustal thin zones and crustal magma bodies that fed the pre-rift flood basalts as well as magma storage and transport zones from active magmatism.

© The Author(s) 2025. Published by Oxford University Press on behalf of The Royal Astronomical Society. This is an Open Access article distributed under the terms of the Creative Commons Attribution License (https://creativecommons.org/licenses/by/4.0/), which permits unrestricted reuse, distribution, and reproduction in any medium, provided the original work is properly cited.

Downloaded from https://academic.oup.com/gji/article/243/1/ggaf282/8211814 by Imperial College of Science Technology and Medicine user on 12 September 2025

New crustal imaging and existing constraints enable us to assess their relative importance in Oligo-Miocene to Recent stretching and magmatism.

The low elevation Turkana Depression comprises a failed, weakly magmatic Mesozoic rift zone now crosscut by Oligo-Miocene to Recent rifts between the uplifted Ethiopia–Yemen and East Africa plateaus (Fig. 1). The unusual 300 km-wide low-lying rift been uplifted since at least 17 Ma and the entire region is dynamically supported by one or more mantle plumes (e.g. Kounoudis *et al.* 2021; Boyce *et al.* 2023; Ogden *et al.* 2023) (Fig. 1). Eocene–Oligocene flood magmatism affected the southwestern part of the Ethiopian plateau bordering the Turkana Depression but there is no evidence for extension until ∼28 Ma (e.g. Davidson & Rex 1980; Ebinger *et al.* 1993; Ragon et al. 2018) (Fig. 2). Geochemical analyses of flood eruptive products between 45–28 Ma show fractionation at progressively shallower crustal levels in crustal magma chambers (Steiner *et al.* 2024). The pre-existing crustal thickness and compositional differences, as well as the variable magma intrusions predict heterogeneities in seismic velocity structure.

The unusual 300 km-wide zone of Oligocene–Miocene to Recent eruptive centres and extensional basins in the Depression, which is three times wider than the rift zones to the north (Main Ethiopian Rift, MER) and south (Eastern Rift, ER), has been interpreted as: (1) rifting into a pre-existing weak zone (e.g. Brune *et al.* 2017; Nutz *et al.* 2022; Pusok *et al.* 2025); (2) along-axis propagation and east–west migration (e.g. Morley *et al.* 1992; Ebinger *et al.* 2000; Corti *et al.* 2019); (3) partial melting of lithospheric drips feeding magmatism (e.g. Furman *et al.* 2016; Morley 2020); and (4) pre-existing oceanic terrane boundaries and failed rift zones, both interpreted as strong zones, but with different characteristics: oceanic terrane boundaries do not localize strain and instead deform diffusively, whereas failed rift zones are circumnavigated and not exploited by the East African Rift (EAR) (Kounoudis *et al.* 2023; Musila *et al.* 2023; Ogden *et al.* 2023; Sullivan *et al.* 2024).The 80–100 km-wide MER to the north is characterized by fault-bounded basins with Quaternary eruptive centres and is underlain by low-velocity crust with >3 km of lower crustal intrusions (e.g. Mackenzie *et al.* 2005; Cornwell *et al.* 2006; Maguire *et al.* 2006). The 60–80 km-wide Eastern rift (south) is also characterized by fault-bounded basins with Quaternary eruptive centres underlain by comparable high bulk crustal Vp/Vs (>1.8; Dugda *et al.* 2005) akin to the magma-mature MER to the north (Stuart *et al.* 2006), indicating significant mafic intrusions. Imaging the distribution and depth extent of magma intrusions, crustal thinning and lateral heterogeneities is essential to evaluate the role of Mesozoic rifting, terrane boundaries and pre-rift magmatism, and to distinguish between the models for the Turkana Depression.

The objectives of our ambient noise tomography study are to characterize the (1) magmatic plumbing systems for the 45–28 Ma flood magmatism; (2) extent of crustal magmatic modification beneath the northern Eastern rift and southern MER and their relation to zones of active deformation; and to (3) evaluate crustal velocity variations associated with the Pan-African terranes and Mesozoic rifts. We integrate information on seismic velocities from previous controlled source and passive source imaging (Mechie *et al.* 1994, 1997; Kounoudis *et al.* 2021, 2023; Ogden *et al.* 2023) and seismic reflection imaging, calibrated by exploration wells, beneath the Turkana Depression (e.g. Winn *et al.* 1993; Schofield *et al.* 2021; Muirhead *et al.* 2022; Kebede et al. 2023). We evaluate the distribution of active (low Vs anomalies) and frozen (fast Vs anomalies) magmatic intrusions associated with the past 45 My of magmatism using high-resolution 3-D Rayleigh shear wave (Vs) velocity models inverted from ambient noise Rayleigh phase velocity recorded by the Turkana Rift Arrays Investigating Lithospheric Structures (TRAILS) project and a few neighbouring stations to the north and south of the study area (Figs 3, 4 and SM1, Supporting Information).

2 GEODYNAMIC AND TECTONIC SETTING

2.1 Geodynamic background

Global tomographic models image one or more mantle plumes rising from the core mantle boundary beneath southern Africa to the base of the lithosphere beneath East Africa (e.g. Ritsema *et al.* 2011; Nyblade 2011; French & Romanowicz 2015; Emry *et al.* 2019; Boyce *et al.* 2023). The entire region, including the Turkana Depression, is dynamically supported (Kounoudis *et al.* 2021; Boyce *et al.* 2023). The Depression's low elevation between the Ethiopian and Kenyan plateaus is thus a consequence of superposition of crustal thinning from multiple phases of rifting (Ogden *et al.* 2023).

The Main Ethiopian and the Eastern rifts developed in ∼120 km-thick lithosphere of the Pan-African orogenic belt accreted to the > 150 km-thick Archaean Tanzania craton (e.g. Emry *et al.* 2019; Afonso *et al.* 2022; Boyce *et al.* 2023) (Figs 1 and 2). Surface expressions of lithospheric heterogeneities in the study area include Pan African (800–500 Ma) accreted terranes and suture zones (e.g. Teklay *et al.* 1998; Stern et al. 2012; Fritz *et al.* 2013) (Fig. 2). The MER and ER are kinematically linked across the southern Ethiopian plateau, and the northern part of the East African plateau through the Turkana Depression (Musila *et al.* 2023; Sullivan *et al.* 2024) (Fig. 1). In southern Ethiopia, the Pan-African accreted terranes include island-arcs, such as a NW-striking oceanic terrane (e.g. Shackleton 1986; Teklay *et al.* 1998; Stern et al. 2012) (Fig. 2); this zone is underlain by high *P*- and *S*-wave velocity mantle lithosphere (<200 km; Kounoudis *et al.* 2021, 2023). Kounoudis *et al.* (2023) suggested that the mantle lithosphere underlying the weakly magmatic Mesozoic Anza rift is underlain by a refractory lithosphere that acted as a rheological boundary to subsequent rifting phases. Pusok *et al.*'s (2025) numerical models of melt percolation revisit conjecture that the Turkana Depression was a lithospheric weak zone in Oligo-Miocene time and ignore the dehydration effects of Mesozoic magmatism and thinned crust, contrary to seismic imaging that indicates the Mesozoic rift zones may have been stronger than the originally 35-40 km-thick crust and 'normal' mantle lithosphere beneath the West Turkana basins at EAR initiation (Kounoudis *et al.* 2023; Ogden *et al.* 2023).

2.2 Tectonic background

The Proterozoic lithosphere beneath the zone of linkage between the MER and ER rifts has been modified in three main rifting phases: the Cretaceous phase (130–80 Ma); a poorly understood Palaeogene phase (65–50 Ma); and Oligocene–Miocene to Recent (28–0 Ma) (Morley *et al.* 1992; Ebinger *et al.* 2000; Torres-Acosta *et al.* 2015). The modified crust encompasses four subparallel Oligocene–Miocene to Recent rift basins: from southwest to northeast and from north to south in each strand: the Turkwel-Lokichar rift, Usno–Omo–Turkana rift, Aluma–Weyto–Chew Bahir–Kino Sogo rift and the Chamo–Segen–Ririba rift, which is the southernmost continuation of the MER (Fig. 1b). In the same region, there are 2–7 km-thick

Downloaded from https://academic.oup.com/gji/article/243/1/ggaf282/8211814 by Imperial College of Science Technology and Medicine user on 12 September 2025

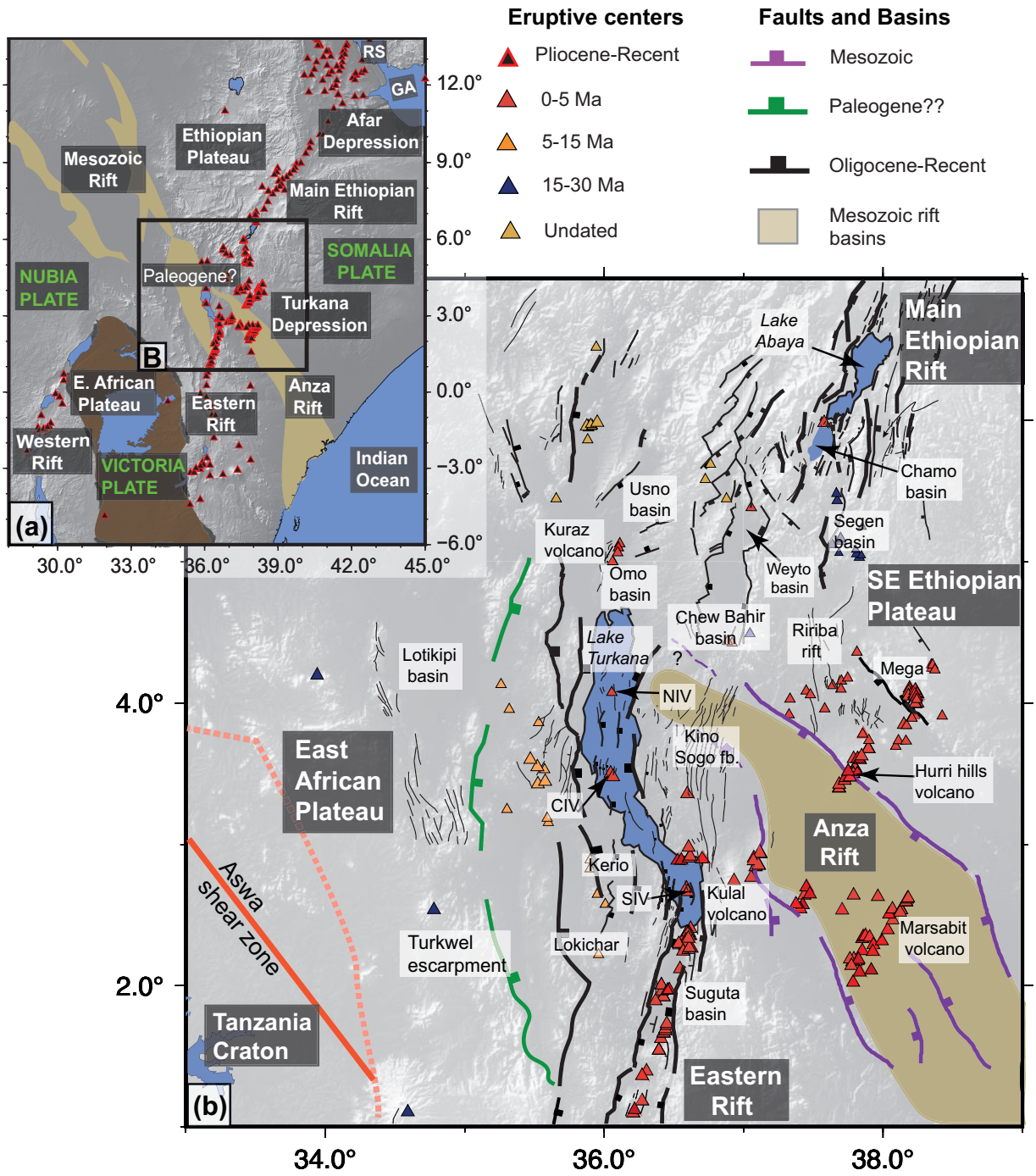


Figure 1. (A) Study region including the Turkana Depression, Main Ethiopian Rift (MER), Eastern Rift (ER) and Western Rift (WR). Mesozoic rifts and enigmatic Paleogene basins are after Bosworth & Morley (1994) and Knappe *et al.* (2020). Pliocene-Recent eruptive centres are after Global Volcanism Program (2013). TZC: Archaean Tanzania craton. RS: Red Sea; GA: Gulf of Aden. (B) Zone of linkage between the MER and ER showing the Turkana Depression with Mesozoic, undated Paleogene or Oligocene and Oligo-Miocene to Recent faults and basins after Morley (2020) and Sullivan *et al.* (2024). Four sub-parallel rift strands from southwest to northeast: Turkwel–Lokichar rift, Suguta-Lake Turkana–Omo–Usno rift, Kino Sogo fault belt (Kino Sogo fb.)-Chew Bahir–Weyto rift and Ririba–Segen–Chamo rift. Kerio basin. Oligocene-Recent eruptive centres are after a compilation by Sullivan *et al.* (2024). The Tanzania craton (orange dashed line) is after Westerhof *et al.* (2014).

Cretaceous sedimentary basins with Palaeogene post-rift sedimentary strata of the weakly magmatic Mesozoic South Sudan and Anza rifts that span the Turkana Depression (e.g. Dindi 1994; Morley *et al.* 1999; Kounoudis *et al.* 2023). Their structural connection remains debated owing to sparse subsurface data and age constraints in South Sudan (e.g. Ebinger & Ibrahim 1994; Hendrie *et al.* 1994; Morley *et al.* 1999).

Mantle plume–lithosphere interactions resulted in 45–28 Ma flood magmatism in the southwestern part of the Ethiopian plateau, and what is now the southern MER (e.g. Davidson & Rex 1980;

Downloaded from https://academic.oup.com/gji/article/243/1/ggaf282/8211814 by Imperial College of Science Technology and Medicine user on 12 September 2025

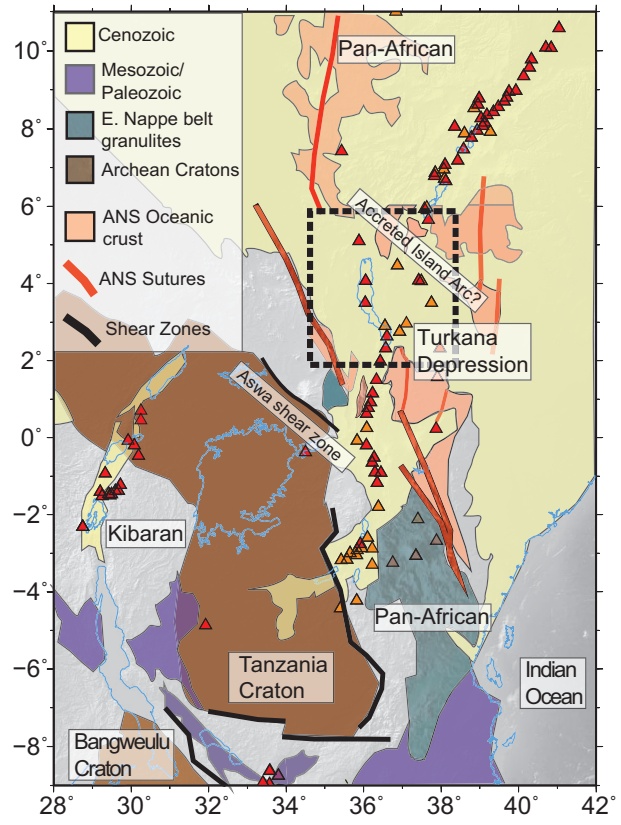


Figure 2. Archaean-Recent tectonic units highlighting Pan-African sutures in red: the 850–620 Ma Arabian–Nubian shield with predominant juvenile Neoproterozoic crust and the 650–620 Eastern Nappe complex with granulite-facies metamorphism (after Fritz *et al.* 2013). Pleistocene (orange) and Holocene (red) volcanoes are denoted by triangles (Global Volcanism Program 2013). Study area is delineated by the black dashed box. ANS is Arabia–Nubia Shield.

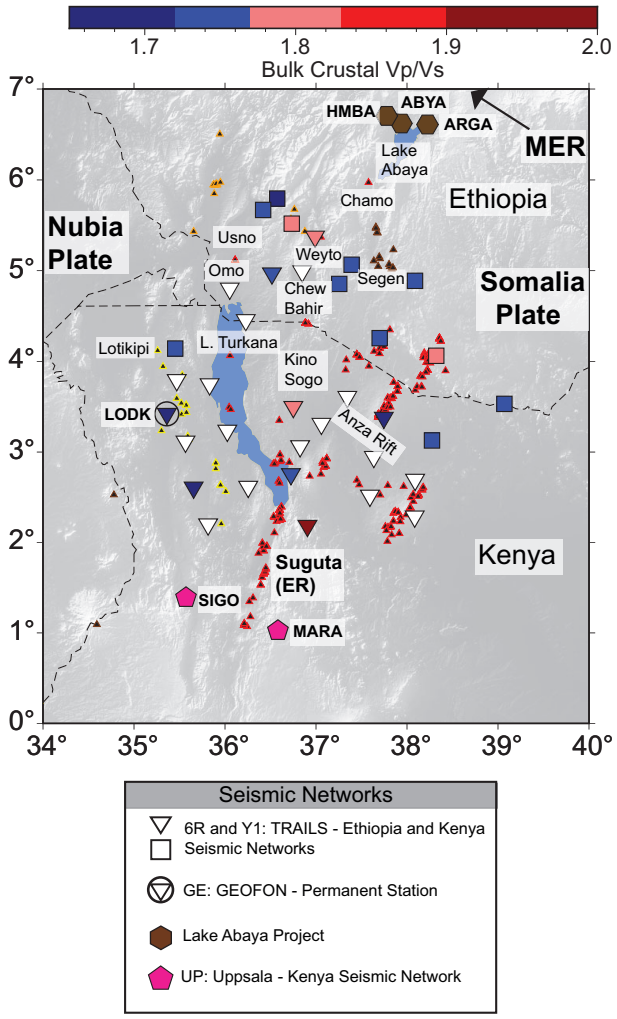


Figure 3. Broad-band seismic stations centred on the Turkana Depression. Pliocene-Recent eruptive centres are after Global Volcanism Program (2013) and Sullivan *et al.* (2024). Squares (Moho depth > 30 km) and inverted triangles (Moho depth < 30 km) are seismic stations that show variations in bulk crustal Vp/Vs (Ogden *et al.* 2023). Inverted triangles: stations with no reliable H-κ stacking result.

Ebinger *et al.* 1993; George *et al.* 1998) (Fig. 1b). Dikes feeding the pre-rift flood basalts (45–28 Ma) must have caused some crustal extension (e.g. Steiner *et al.* 2021), but no tilting or basin formation has been documented before ∼27 Ma (e.g. Davidson & Rex 1980; Ebinger *et al.* 2000; Erbello et al. 2024). The southern extent of the flood basalts is 5.5°N (Steiner *et al.* 2021).

Between 32–27 Ma, there was a pulse of basaltic volcanism followed by the initiation of faulting west of Lake Turkana at ∼27 Ma, leading to the formation of half-graben basins (Morley *et al.* 1999; Wescott *et al.* 1999; Ragon et al. 2018). Based on published seismic reflection data calibrated by well data, the westwards-tilted Lokichar basin contains 3–7 km of Oligo-Mid-Miocene to Recent sedimentary and volcanic strata (Morley *et al.* 1992; Schofield *et al.* 2021). By Mid-Miocene time, strain and magmatism had jumped eastward to the present-day Lake Turkana rift, which contains 2–5 km of sedimentary strata with localized magmatic intrusions (Dunkleman *et al.* 1989; Muirhead *et al.* 2022). East of Lake Turkana, there are unfaulted 3 Ma-Recent basaltic shield complexes and monogenetic cones overlying <5 km of Mesozoic strata (e.g. Winn *et al.* 1993; Guth 2016) (Fig. 1b). The 27 Ma-Recent eastward migration and abandonment of magmatism and faulting produced the unusual breadth of the East African rift system in northern Kenya, but only the ∼100 km-wide Lake Turkana basin is currently seismically and volcanically active (e.g. Morley *et al.* 1992; Knappe *et al.* 2020; Musila *et al.* 2023; Sullivan *et al.* 2024). In southern Ethiopia, the ∼ 250 km-wide zone of active deformation between the Turkana rift and the MER has narrowed with the eastwards migration of rifting, and current linkage is achieved by short oblique-slip and strike-slip faults at the tips of N–S to NNE-striking extensional fault arrays, creating a broad transtensional shear zone in southwestern Ethiopia (Sullivan *et al.* 2024). Quaternary magmatism occurs in the seismically active Turkana rift, and the largely unfaulted regions east of the lake (Fig. 1). The diachronous magmatism and faulting spanning >30 My, strong, and refractory mantle beneath the Anza rift (Kounoudis *et al.* 2023) argue against the lithospheric drip model (e.g. Furman *et al.* 2016) and contradict initial conditions of the Mesozoic rift as a pre-existing weak zone (e.g. Brune *et al.* 2017; Pusok *et al.* 2025).

2.3 Previous crustal seismic studies

Passive and controlled source studies provide constraints on crustal velocity structure beneath the study area (e.g. Mechie *et al.* 1994; Prodehl *et al.* 1994; Benoit *et al.* 2006; Kounoudis *et al.* 2023;

Downloaded from https://academic.oup.com/gji/article/243/1/ggaf282/8211814 by Imperial College of Science Technology and Medicine user on 12 September 2025

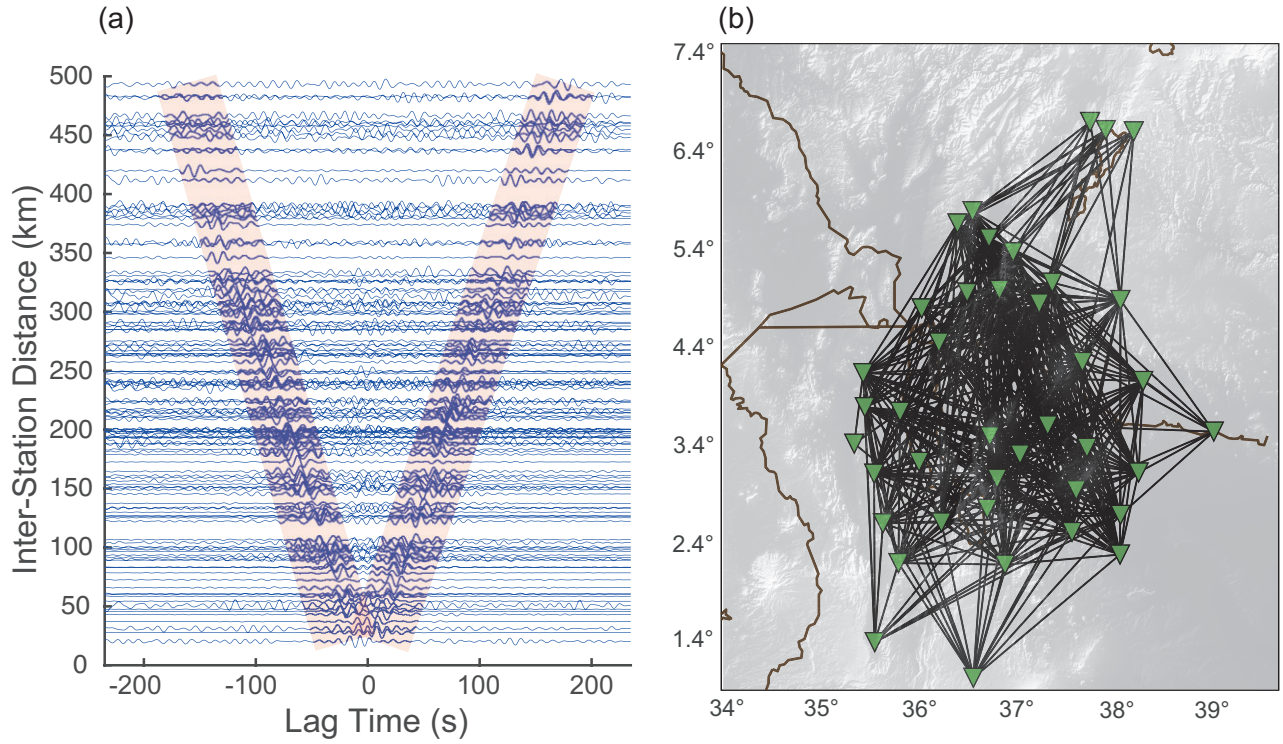


Figure 4. (A) Vertical–vertical Rayleigh wave cross-correlation moveouts that are filtered between 0.05–0.12 Hz, plotted as a function of interstation distance and lag time. (B) Spatial distribution of 9 s period station pairs that have Noise Correlation Functions with SNR > 5.0 and are as lines. Broad-band seismic stations are shown as inverted triangles.

Ogden *et al.* 2023). North of our study area, a wide-angle seismic study (Maguire *et al.* 2006) and ambient noise tomography studies of the magma-mature MER provide a strong comparative basis (Kim *et al.* 2012; Chambers *et al.* 2019, 2021; Alemayehu *et al.* 2023). South of the Depression, the Eastern rift has comparable high bulk crustal Vp/Vs akin to the magma-mature MER to the north, indicating significant mafic intrusions (e.g. Dugda *et al.* 2005). Receiver function analyses and surface wave studies using data from the TRAILS network and nearby seismic stations reveal Moho depths within the Depression of 21–30 km relative to the 34–38 km in unrifted areas west and east of the TRAILS array (Fig. 3) (Kounoudis *et al.* 2023; Ogden *et al.* 2023). The thinnest crust underlies the Lokichar, Omo-Turkana, Kino Sogo and Weyto-Chew Bahir rifts, all of which lie within or along the margin of the Mesozoic Anza rift; crustal stretching factors in these areas are $\geq$1.9 (Ogden *et al.* 2023). Despite the 45 My history of magmatism in some parts of the study area, the discrete bulk crustal Vp/Vs in most of the region is 1.74, except in some localized regions east of Lake Turkana where Vp/Vs of >1.8 (Fig. 3) that may signify the influence of Miocene-Recent magmatic modification (Musila *et al.* 2023; Ogden *et al.* 2023) and/or pre-existing ultrabasic and high-grade metamorphic rocks (e.g. Dodson 1963; Mosley 1993; Fritz *et al.* 2013).

3 DATA

We use seismic data collected by 34 broad-band seismic stations from the TRAILS project. The TRAILS network spans southwestern Ethiopia (network 6R, Bastow 2019) and northwestern Kenya (network Y1, Ebinger 2018) and recorded continuously from January 2019 to June 2021 (Fig. 3). The combined network comprised Güralp CMG-3T (in Kenya) and CMG-ESP (in Ethiopia) instruments recording at 50–100 samples per second. Additional data were sourced from permanent broad-band, STS2 station LODK (network GE) west of Lake Turkana, CMG-3T stations MARA and SIGO (network UP) south of our study area and three CMG-6TD sensors in southern Ethiopia (ABYA, ARGA, HMBA; Ogden *et al.* 2021) (Fig. 3). The combined seismic network comprised 40 stations spanning a 300 km-wide zone of linkage between the MER and ER with an average station spacing of 30–40 km, centred on the Turkana Depression, with the stations 50–100 km north and south of the array used to better localize anomalies.

4 METHODS

4.1 Computing cross-correlations

Instrument responses were removed from day-long seismograms of all 40 broad-band stations (Figs 3, 4b and SM1, Supporting Information) for the time period 2019–2021. The resulting waveforms were Butterworth bandpass filtered with corner frequencies of 0.01 and 8 Hz, whitened, and 1-bit normalized before the computation of the cross-correlations (e.g. Bensen *et al.* 2007; Civilini *et al.* 2019). The daily cross-correlations for each station pair were computed according to Lecocq *et al.* (2014), following the processing workflow outlined in Bensen *et al.* (2007). The computed cross-correlations are the diagonal components of the Green's function matrix for Rayleigh waves (vertical–vertical, ZZ) (Fig. S2, Supporting Information). Dispersive surface waves are not observed in the

Downloaded from https://academic.oup.com/gji/article/243/1/ggaf282/8211814 by Imperial College of Science Technology and Medicine user on 12 September 2025

off-diagonal components of the Green's function tensor (e.g. ZT) so were excluded from further analysis (e.g. Lin *et al.* 2008; Civilini *et al.* 2019).

At each station pair, we performed linear stacking on one-hour segments of the day-long seismic traces containing the recorded ambient noise signal resulting to the daily Noise Correlation Functions (NCFs). The daily NCFs at each station pair were further stacked to improve the signal-to-noise (SNR) ratios. The dispersive surface waves' signals are differentiated from the 'noise' in the seismic traces by using lag times faster and slower than 2 km s^{-1}, respectively (Fig. S2, Supporting Information). SNR is calculated by dividing the peak amplitude value of the dispersive surface waves with the root mean square (RMS) of the 'noise' parts in the day-long seismic trace. Station pairs with stacked NCFs with signal-to-noise ratios > 5.0 are then used to extract the Rayleigh wave dispersion curves.

4.2 Frequency time analyses (FTAN)

Prior to computing the dispersion curves using frequency–time analysis (FTAN; Levshin *et al.* 1972, 1989), we flipped and stacked the acausal (negative) to the causal (positive) part of the station pairs' cross-correlations to further improve the SNR of the stacked NCFs (Fig. S2, Supporting Information). Flipping and stacking was done after visually inspecting each of the station pairs' stacked NCFs to ensure that their causal and acausal parts are symmetric. The FTAN method (Levshin *et al.* 1972, 1989) was then used to extract dispersion curves in the frequency domain from time-series seismic data, which in our case are the flipped and stacked NCFs.

FTAN computes group velocity dispersion curves using a sliding Gaussian filter in the frequency domain of the stacked NCFs. Phase velocities are then calculated from the envelope function of the group velocity and the phase of the analytical signal (e.g. Snieder 2004; Bensen *et al.* 2007). Since we lacked a baseline Rayleigh phase velocity curve in the Turkana Depression, we generated one using the region's 1-D *P*-wave velocity model inverted from local earthquakes (Musila *et al.* 2023) and bulk crustal Vp/Vs of 1.74 (Ogden *et al.* 2023) to generate a 1-D *S*-wave velocity model. We then took 92 per cent of the derived 1-D *S*-wave velocity model to generate our reference Rayleigh phase velocity curve (e.g. Lin *et al.* 2008). At each station pair, the newly computed reference Rayleigh dispersion curves were then used to pick the nearest phase velocity curve branches across all periods of interest: 5–25 s.

While the quality of dispersion curves relies on the SNR of the stacked NCFs at each station pair, we further incorporate our dispersion curve management criteria in our processing workflow to select the dispersion curves used in this study. The criteria used is based on theory, literature (e.g. Civilini *et al.* 2023), and our seismic network geometry (Figs 3, 4 and SM1, Supporting Information). (1) At all periods, phase velocity dispersion curves should be faster than the group velocity dispersion curves with the caveat that phase velocities might become smaller than group velocities in crust with pronounced low-velocity zones at depth. (2) Dispersion curves computed from the NCFs and whose station pair distances are shorter than the surface waves' 2-wavelength criterion, at all periods, are discarded (e.g. Shapiro *et al.* 2005; Brenguier *et al.* 2007). (3) If the first period in the dispersion curve was $\geq$10 s, we discard the curve unless the station pair distance is $\geq$500 km. (4) At all periods, phase velocities of the dispersion curves should be 2–5 km s^{-1}, a range that mostly isolates the dispersive surface wave signals (e.g. Civilini *et al.* 2019) (Fig. S2, Supporting Information).

In this study, we only present Vertical–Vertical (ZZ) Rayleigh wave dispersion curves. The RR Rayleigh dispersion curves are relatively few in number, irregularly spaced and have relatively low SNR values across the study area (Fig. S6, Supporting Information). It, therefore, makes it difficult to obtain a set of parameterizations needed to invert for representative RR Rayleigh period and shear wave (Vs) models required to address the objectives of this study. ZZ Rayleigh dispersion curves, however, are plentiful, uniformly distributed, and have significantly higher SNR values in comparison (Figs 4b, 5b and SM6, Supporting Information); this explains why our ZZ Rayleigh period and their subsequent Vs models have representative models that have better lateral and depth resolutions.

4.3 Sensitivity kernels

We use the *senskernel* software package, building on Levshin *et al.* (1989), to determine the sensitivity kernels of the surface wave's phase velocities at different periods. The computation of sensitivity kernels requires input shear wave velocity and density models that are representative of the study area. We use a 1-D *P*-wave velocity model inverted from the phase arrival times of local earthquakes located in the Turkana Depression (Musila *et al.* 2023) (Fig. 5a). Using the local 1-D *P*-wave velocity model and the bulk crustal Vp/Vs estimate of 1.74 (Ogden *et al.* 2023), we determine a 1-D shear velocity model, with densities determined following the Brocher (2005) empirical relations between wave speeds and density. We then determine the sensitivity kernels using parameters such as shear wave velocity and density variations at depth and taking the partial derivative of the surface wave's phase velocity with respect to shear wave velocity at depth ($\delta c/\delta b$) (e.g. Levshin *et al.* 1972). We use the computed phase velocity sensitivity kernels to describe the sensitivity of Rayleigh wave phase velocities as a function of depth (Fig. 5b).

4.4 Surface wave inversion

The 'nearly linear' tomographic algorithm of Barmin *et al.* (2001) is used to estimate the 2-D surface wave phase velocity variations across the region by inverting the dispersion curves that have passed our dispersion curve management criteria (Section 4.2). The tomographic algorithm inverts the traveltime residuals to estimate the surface wave velocity variations along each station pair path. The algorithm uses spherical geometry, nodes, and dispersion curve density to set up the parametrization and regularization needed for the inversion process (Barmin *et al.* 2001). We used a grid node spacing of 0.2° to invert 150–470 ray paths across 5–25 s periods (Figs 4 and 6).

The user-defined regularization parameters include the width of the Gaussian smoothing filter (δ) and the degree of amplitude smoothing (α) that depends on the nodal spacing and interstation distance. However, for this study, we took a step further and chose our final set of regularization parameters by performing a trade-off curve analysis. This involves plotting the inverted models' residuals, at all periods, with their respective smoothing parameters. Based on the ZZ Rayleigh trade-off curve analyses, we chose model regularization parameters at the inflection point of our trade-off curve plot resulting to $\delta = 45$ and $\alpha = 340$ (Fig. S7, Supporting Information). We then use the regularization parameters in our model resolution tests (Fig. 6) and inversion of our Rayleigh wave period maps (Fig. 7).

Downloaded from https://academic.oup.com/gji/article/243/1/ggaf282/8211814 by Imperial College of Science Technology and Medicine user on 12 September 2025

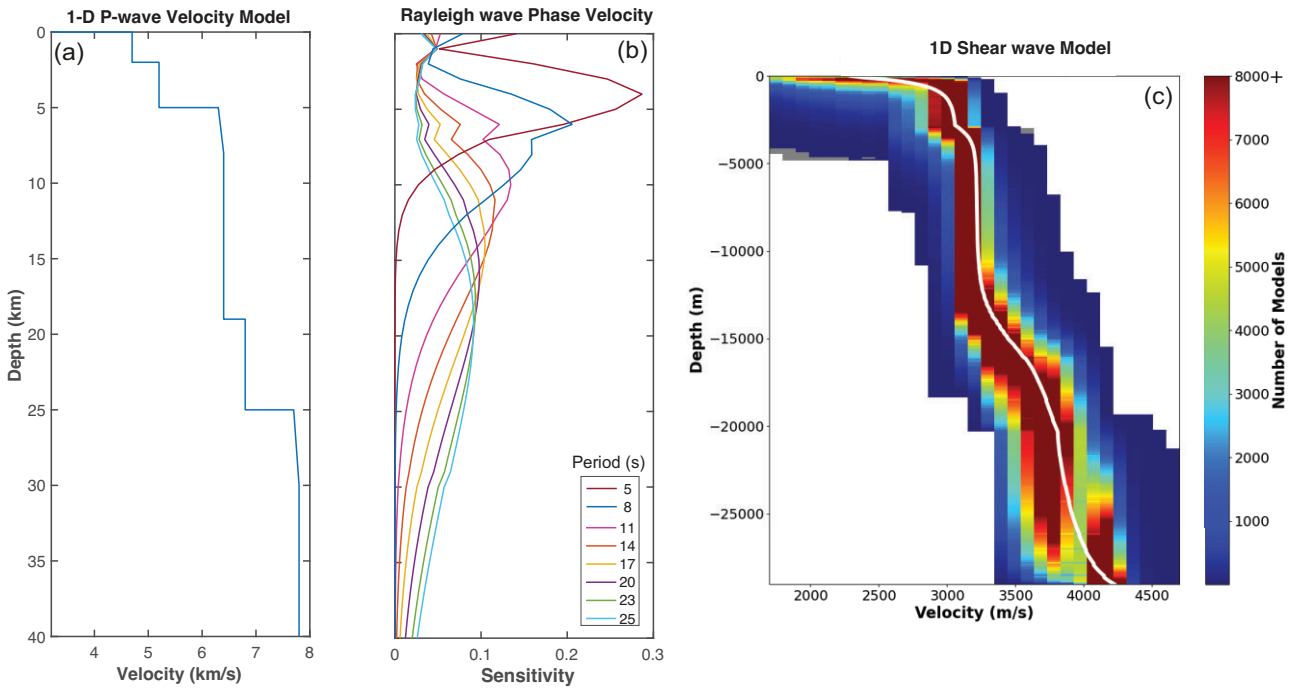


Figure 5. (A) Average 1-D *P*-wave velocity model inverted from arrival times of local earthquakes in the study area from 2019–2021 (Musila *et al.* 2023). (B) Sensitivity kernels of Rayleigh waves at selected periods in seconds. (C) Example of 1-D shear wave model in Lake Turkana where blue–green–yellow–red are accepted models that provide a ≤10 per cent misfit to the extracted depth dispersion curves at each node; the grey models are below the misfit threshold. White solid line: the weighted mean for all blue–green–yellow–red accepted models.

4.4.1 Model resolution

We conducted several tests to assess the resolution of our phase velocity tomographic models at 9 and 22 s (Fig. 6). We calculate interstation velocities across synthetic models comprising high (3.5 km s^{-1}) and low (3.0 km s^{-1}) velocity anomalies. The synthetic models include (1) regularly spaced circular patches of low-velocity anomalies representing the sedimentary basins in the study area (Fig. 1b); and (2) localized regions of low-velocity anomalies, depicting sedimentary basins or active crustal magma bodies (Fig. 6). In all the synthetic models, we add 0.02 km s^{-1} Gaussian noise to mimic the actual noise levels in our ambient noise observations (e.g. Kounoudis *et al.* 2023). We compute the synthetic phase velocities using Fatiando, an open-source Python library for geophysical inversions (Uieda *et al.* 2013). The computed synthetic phase velocities are then inverted using the same algorithm (Barmin *et al.* 2001) with the same regularization parameters described in Section 4.4. In southern MER, at Abaya and Chamo basins, resolution tests indicate that we cannot resolve anomalies due to a paucity of cross-cutting station pairs (c, d, e and f, Fig. 6). We, therefore, exclude this southern MER region in our subsequent analysis and interpretations. However, we retain data from the three northernmost seismic stations because they boost resolution below the Depression (Fig. 6).

4.5 Shear wave velocity inversion

We use a grid-search algorithm to extract surface wave velocity values at each latitude–longitude grid node, with 0.2° grid spacing, at all periods on the inverted surface wave velocity maps. We refer to these extracted surface wave velocity values at all periods in each grid node as our 'pseudo-dispersion curves' (Figs S3, SM4 and SM5, Supporting Information). The extracted pseudo-dispersion curves are then inverted to 1-D shear wave velocities using Dinver's neighbourhood algorithm (Sambridge 1999; Wathelet *et al.* 2004, 2005, 2008). The neighbourhood inversion algorithm requires an input 1-D layered model with variations of *P*- and *S*-wave velocities at depth, and the layers' interface depths (Table SM1, Supporting Information). The density range at each layer was kept constant as it has been shown to have minor influence on the resulting dispersion curve (Wathelet 2008). The number of layers chosen in the 1-D model (Table SM1, Supporting Information) is consistent with the number of crustal layers imaged by a wide-angle seismic profile along the Lake Turkana basin (Mechie *et al.* 1994, 1997), and the 1-D *P*-wave model velocity model inverted using arrival time of local earthquakes in the region (Fig. 5a; Musila *et al.* 2023).

For each depth dispersion curve at each grid point, we use Dinver's probabilistic neighborhood algorithm to invert for 1-D shear wave velocity models with maximum depths of 29 km that minimize the misfit values (Fig. 5c). The misfit values are determined as a percentage difference between the extracted pseudo-dispersion curve and the calculated dispersion curves obtained from forward modelling of the inverted 50 000 probabilistic 1-D shear wave velocity models at each grid point. All the final 1-D Vs models used in the subsequent analysis have ≤ 10 per cent misfit from the extracted pseudo-dispersion curve at each node. We take the weighted mean for all the accepted 1-D inverted models at each node to assess the likelihood of the inverse solution in a comprehensive manner (Figs 5c and SM8, Supporting Information). Lastly, the weighted shear wave velocities at each latitude–longitude node are joined to form a volumetric description of shear wave velocity variations at depth: a pseudo-3-D velocity structure model. From our new

Downloaded from https://academic.oup.com/gji/article/243/1/ggaf282/8211814 by Imperial College of Science Technology and Medicine user on 12 September 2025

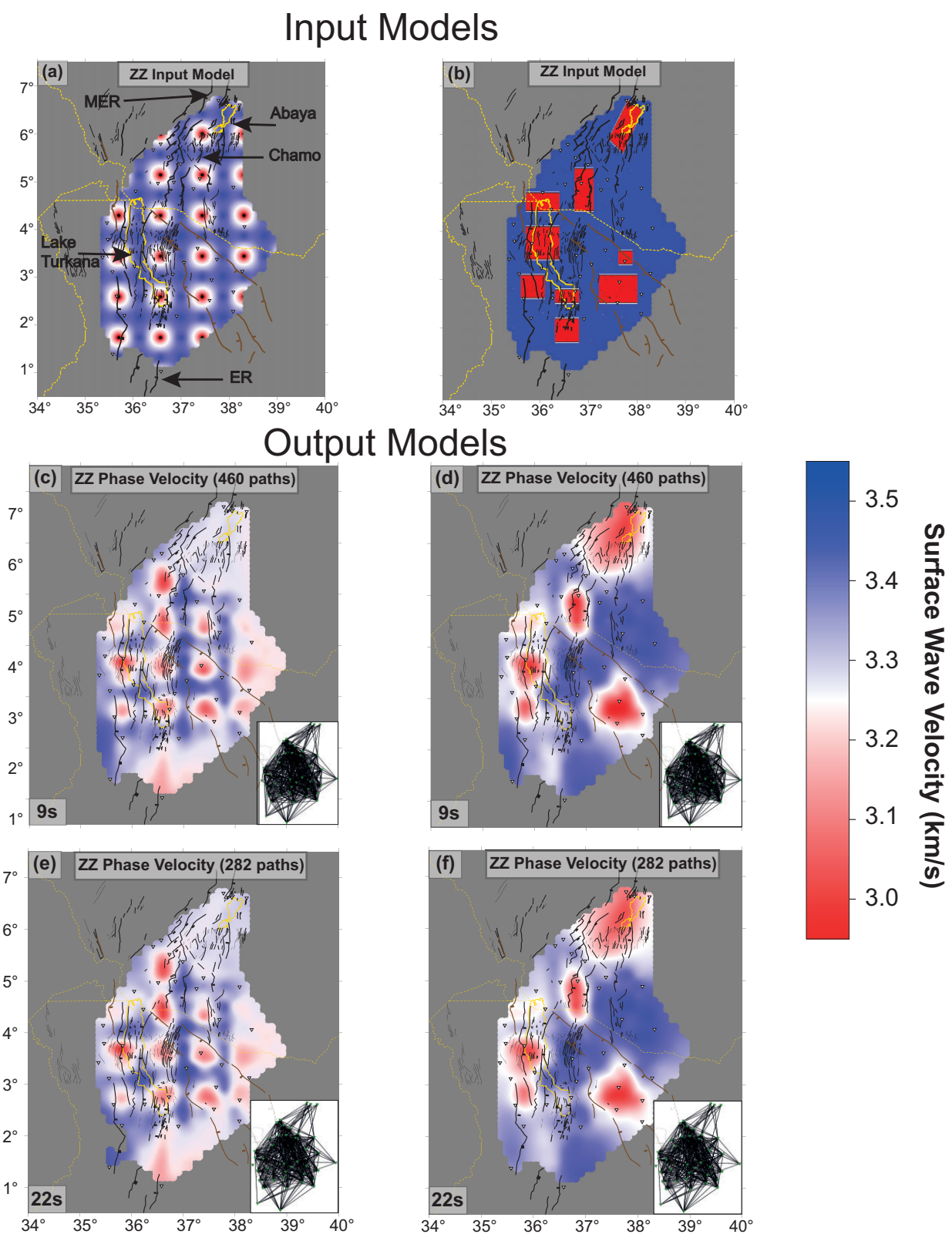


Figure 6. Rayleigh wave resolution test results. Our input models include checkerboard tests with 0.4° cell size that is roughly equivalent to our station spacing (**a**). We also include input models that represent sedimentary basins and potential crustal magma bodies in the study area **(b)**. Resolution test results **(c, d, e and f)** are obtained using the same station pair coverage (dispersion curves), and regularization parameters as in our observed data isotropic inversions as shown in Fig. 7.

Downloaded from https://academic.oup.com/gji/article/243/1/ggaf282/8211814 by Imperial College of Science Technology and Medicine user on 12 September 2025

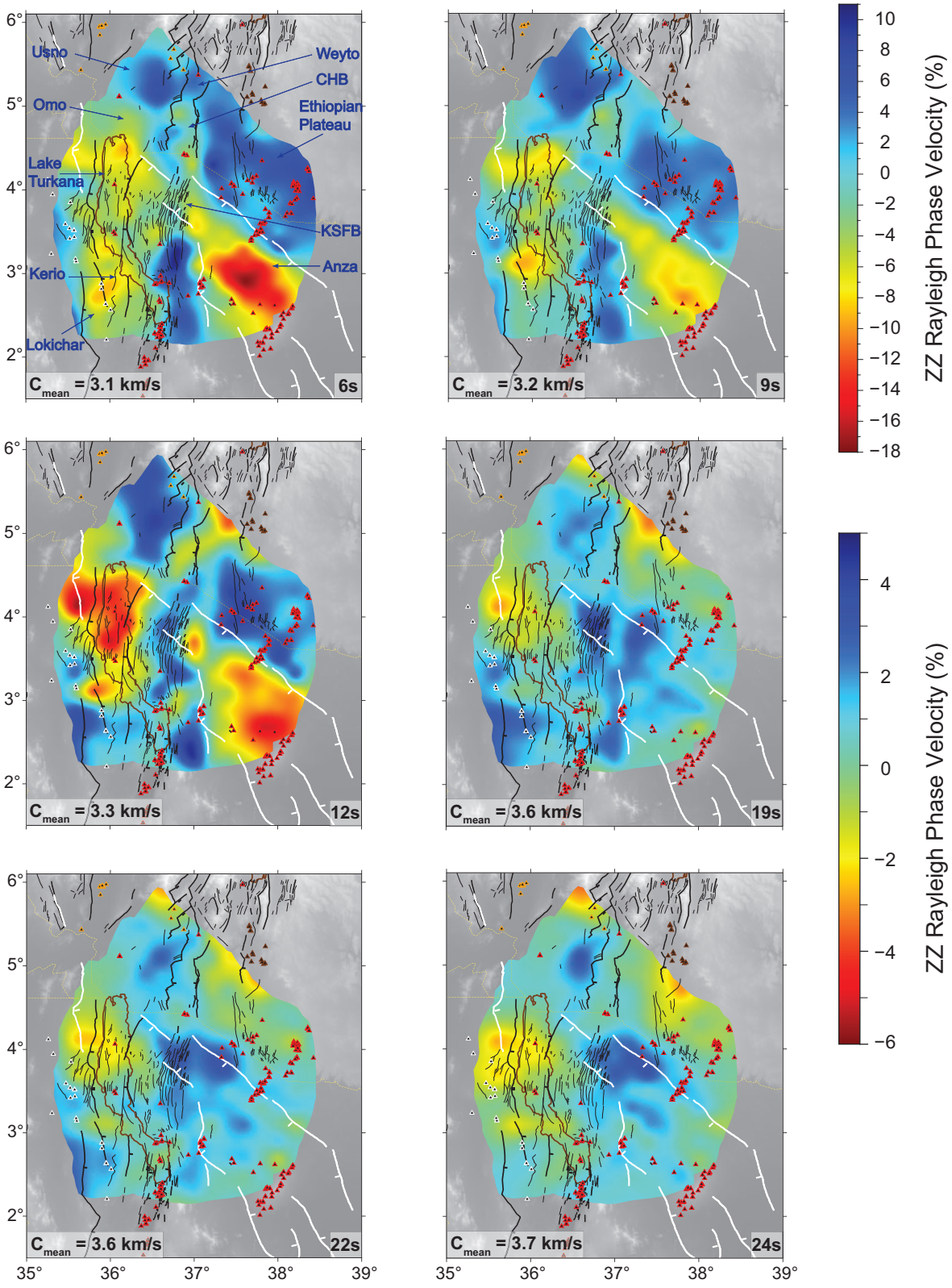


Figure 7. Rayleigh-wave phase velocity as a percentage difference from the mean phase velocity (C_{mean}) inverted using vertical–vertical cross-correlations for periods ranging from 5 to 24 s. Mesozoic-Paleogene and Oligo-Miocene to Recent faults are in white and black, respectively (Sullivan *et al.* 2024). Eruptive centres are triangles colour coded by age as in Figure 1 (Sullivan *et al.* 2024).

Downloaded from https://academic.oup.com/gji/article/243/1/ggaf282/8211814 by Imperial College of Science Technology and Medicine user on 12 September 2025

pseudo-3-D model, we derive depth slices and cross-sections to investigate shear wave velocity variations at depth along profiles of interest.

5 RESULTS

5.1 2-D Phase velocities

5.1.1 Low-velocity anomalies at 5–9 s

Velocity variations are greatest at shorter periods of 5–9 s that sample shallow, heterogeneous crust (Fig. 7). The low-velocity anomalies (−8 to −18 per cent deviation from $C_{mean} = 3.1–3.2$ km s^{-1}) coincide with the failed Mesozoic Anza rift. The Oligocene–Miocene to Recent Omo, Lake Turkana, Lokichar and Kerio basins also have relatively low-velocity anomalies (−4 to −10 per cent deviation from C_{mean} of 3.1–3.2 km s^{-1}) at shorter periods of 5–9 s (Fig. 7). Weyto and Chew Bahir rift basins in SW Ethiopia reveal low-velocity anomalies (−3 to −6 per cent deviation from C_{mean} of 3.1–3.2 km s^{-1}) at periods of 5–9 s.

5.1.2 High-velocity anomalies at 5–9 s

Zones with high-velocity anomalies (3–12 per cent deviation from C_{mean} of 3.1–3.2 km s^{-1}) coincide with (1) regions covered by Eocene–Oligocene flood basalts in southwestern Ethiopia (e.g. Davidson & Rex 1980; George *et al.* 1998; Ebinger *et al.* 2000; Steiner *et al.* 2021), (2) meta-basic rocks in one or more Pan-African accreted terranes (Dodson 1963; Mosley 1993; Fritz *et al.* 2013) and/or (3) un-rifted sections of the Ethiopian plateau (Fig. 7).

5.1.3 Low-velocity anomalies at 12–24 s

Regions of superposed Mesozoic-Paleogene and Oligo-Miocene to Recent rifting phases such as the northern and central zones of the Omo-Turkana rift have relatively low-velocity anomalies (−2 to −6 per cent deviation from C_{mean} of ≥ 3.6 km s^{-1}) at 12–24 s periods; at the same period range (Fig. 7).

5.1.4 High-velocity anomalies at 12–24 s

Areas with the shallowest Moho depths (≤25 km) in the region are basins west of Lake Turkana, the Kino Sogo Fault Belt and the Anza rift basins (Ogden *et al.* 2023). All these crustal thin zones have high-velocity anomalies (2–5 per cent deviation from C_{mean} 3.3–3.7 km s^{-1}) at 12–24 s periods (Fig. 7).

5.2 3-D Shear wave velocities

From the inverted 3-D Rayleigh Vs models, we extract cross-sections to investigate shear wave velocity variations and their correlations with pre-existing accreted terranes, sedimentary basins, Quaternary volcanoes and pre-rift flood basalts (Figs 1 and 2). Our Vs models were inverted using a 0.2° grid spacing, consistent with the inverted period models. The final model has a resolution to depths of ∼30 km (Figs 8 and 9).

In our 3-D Vs depth cross-sections, regions in the crust with Vs ≤ 2.6 km s^{-1} are bounded by green dashed contour lines; this velocity contour matches with depth to crystalline basement in rift basins where seismic reflection and well data are available (e.g. Winn *et al.* 1993; Schofield *et al.* 2021; Kebede et al. 2024). The region's background crustal shear wave speed values were determined using *P*-wave crustal velocity models from the Kenya Rift International Seismic Project (KRISP) wide-angle study (Mechie *et al.* 1994, 1997), combined with a 1-D *P*-wave velocity model inverted from local earthquakes in the region (Musila *et al.* 2023) and a bulk crustal Vp/Vs ratio of 1.74 (Ogden *et al.* 2023). The background Vs isovelocities are overlain on the 3-D Vs models to help assess local variations of the Vs structure along profiles of interest (Fig. 9). The upper crust and mid-lower crust are defined as Vs ≤ 3.2 and 3.4–3.6 km s^{-1}, respectively. We approximate the Moho depth to be between 3.8–4.0 km s^{-1} contour line as highlighted by Kounoudis *et al.* (2023), and validate, where available, with Moho depth estimates from refraction/wide-angle reflection (Mechie *et al.* 1994, 1997) and H-κ receiver function results (Ogden *et al.* 2023). We extracted cross-sections to compare velocity variations with areas of flood magmatism, crustal stretching, pre-existing crustal compositional variations and active magmatism (Fig. 9).

The assumptions made when identifying the high- and low-velocity zones (HVZs and LVZs) in our 3-D Vs models are as follows: (1) The HVZs are interpreted as ∼3.8 km s^{-1} zones at crustal depths, assuming the Ogden *et al.* (2023) Moho depths (HVZ1, HVZ2 and HVZ3, Fig. 9). (2) Crustal LVZs can be manifested at shallow and/or mid-lower crustal depths. For shallow LVZs associated with the sediments in Mesozoic-Paleogene and Oligocene–Miocene to Recent rift basins, we consider a velocity contour of Vs ≤ 2.6 km s^{-1} consistent with depth to crystalline basement as determined by exploratory wells in the rift (e.g. Winn *et al.* 1993). Mid-to-lower crustal LVZs, our focus, are identified as zones with velocity reduction of Vs ≤ 3.4 km s^{-1} at mid-lower crustal depths (8–20 km depth). Additionally, these mid-lower crustal LVZs are also compared to surface geology (e.g. Quaternary eruptive centres) and active crustal strain zones in the region (Musila *et al.* 2023). In the active rift zone where strain is localized (e.g. in the Turkana rift), the identified mid-lower crustal LVZs have pipelike clusters of earthquakes with some LVZs overlain by Quaternary eruptive centers (LVZ1 in Profiles C–C′ and E–E′, Fig. 9). The other identified group of mid-lower crustal LVZs are in the seismically inactive zones that are overlain by Holocene-Recent eruptive centers east of the Lake Turkana rift (LVZ2 in Profile F–F′, Fig. 9). Lastly, all similar HVZs and LVZs sampled by multiple profiles are herein identified by same name (e.g. LVZ1 sampled by both Profiles C–C′ and E–E′ so as HVZ2 in Profiles B–B′ and F–F′).

5.2.1 Broadly rifted zone in southern MER

In the Broadly Rifted Zone (BRZ) of southernmost Ethiopia, Neoproterozoic crustal domains associated with the Pan-African oceanic terranes are adjacent to regions of 45–28 Ma flood basalts (e.g. Davidson & Rex 1980; Ebinger *et al.* 1993; George *et al.* 1998) (Fig. 2). The Neoproterozoic oceanic crustal domains are underlain by high-velocity anomalies (Vs of ≥ 3.6 km s^{-1}) up to depths of 6–7 km (A–A′ and B–B′, Fig. 9). A more localized (≤50 km-wide), 10–15 km-thick, mid-lower crustal, fast wave speed (Vs ≥ 3.8 km s^{-1}) zone at ≥15 km depth (HVZ1 in B–B′, Fig. 9) is interpreted as an Eocene–Oligocene crustal feeder zone for flood magmatism. These localized fast wave speeds are consistent with imaged lower crustal layered frozen sills as observed in the heavily intruded and underplated MER to the north (e.g. Mackenzie *et al.* 2005; Maguire *et al.* 2006). East of the flood basalt province, we observe low upper

Downloaded from https://academic.oup.com/gji/article/243/1/ggaf282/8211814 by Imperial College of Science Technology and Medicine user on 12 September 2025

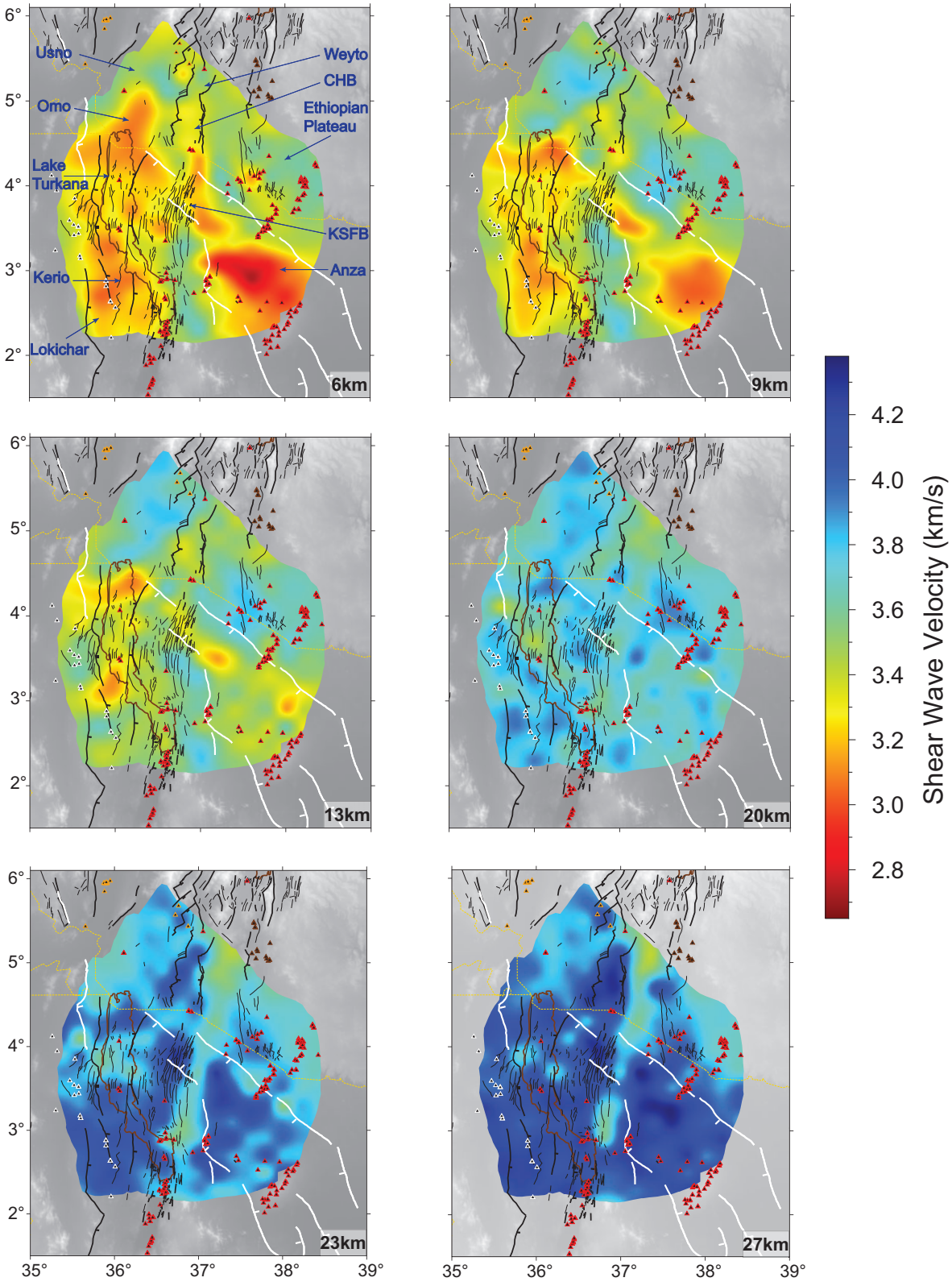


Figure 8. Absolute shear wave velocity depth slices inverted from the ZZ Rayleigh waves period maps. Mesozoic-Paleogene and Oligo-Miocene to Recent faults are in white and black, respectively (after Sullivan *et al.* 2024). Eruptive centres are triangles colour coded by age as in Figure 1 (Sullivan *et al.* 2024).

Downloaded from https://academic.oup.com/gji/article/243/1/ggaf282/8211814 by Imperial College of Science Technology and Medicine user on 12 September 2025

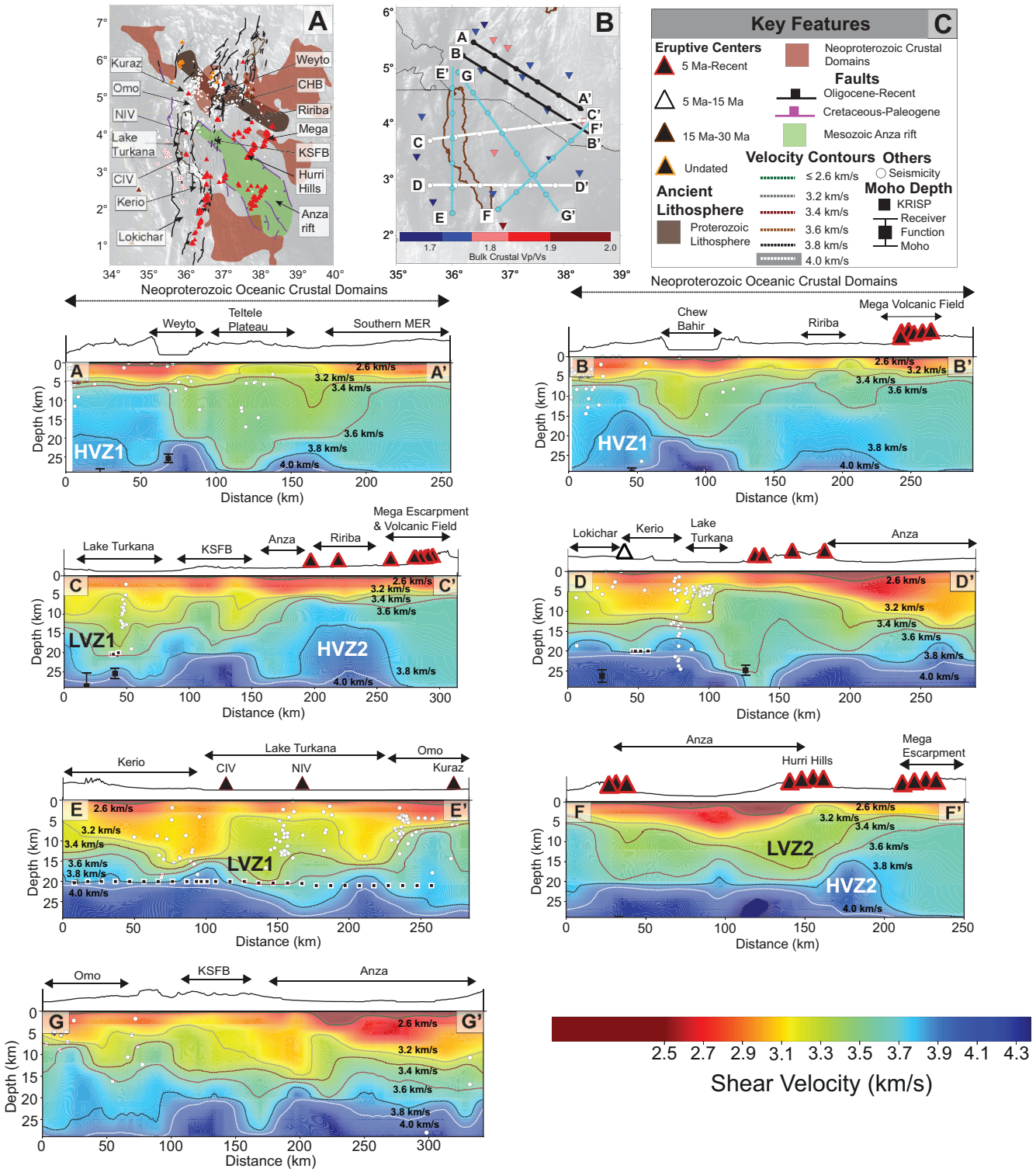


Figure 9. Shear wave cross-sections through the Turkana Depression extracted from ZZ Rayleigh 3-D shear wave models across profiles (A–G). Black boxes with white outlines are Moho depths from Kenya Rift International Seismic Project (KRISP) refraction wide-angle reflection seismic studies (e.g. Mechie *et al.* 1994). Moho depths constrained by receiver functions are in boxes with error bars (Ogden *et al.* 2023) and the polygons show KRISP results. The earthquakes are projected from 5 km on either side of the cross-sections (Musila *et al.* 2023). The topography has 1:15 vertical exaggeration. Depth resolution for our ZZ Rayleigh 3-D shear wave models is 27 km. (B) H-κ stacking results on the discrete bulk crustal Vp/Vs from are from Ogden *et al.* (2023).

Downloaded from https://academic.oup.com/gji/article/243/1/ggaf282/8211814 by Imperial College of Science Technology and Medicine user on 12 September 2025

to mid-crustal velocity of 3.4 km s^{-1} beneath the actively deforming Chew Bahir and Segen rift basins (A–A′ and B–B′, Fig. 9).

5.2.2 Omo-Turkana rift

The Omo-Lake Turkana rift is characterized by the Quaternary eruptive centres of Kuraz, North (NIV), Central (CIV) and South Island (SIV) volcanoes (Fig. 1b). Active deformation is localized to this ∼100 km-wide part of the Turkana Depression where geodetic strain rate is two orders of magnitude larger than seismic strain rate, suggesting aseismic deformation (e.g. active magma intrusion) accommodates a significant proportion of modern-day extension (Musila *et al.* 2023). Along the axis of the Lake Turkana rift, localized low velocity zones (Vs of ∼3.4 km s^{-1}) reach 20 km depth, coincident with the NIV and CIV eruptive centres, several of which have pipe-like earthquake clusters throughout the crust (**LVZ1** in Profiles **C–C′** and **E–E′**, Fig. 9). These localized low-velocity anomalies coincide with magma intrusions imaged by seismic reflection data along the Lake Turkana rift (Dunkleman *et al.* 1989; Schofield *et al.* 2021; Muirhead *et al.* 2022). The low Vs and geometry is similar to observations in the active rift segments of the MER to the north (e.g. Chambers *et al.* 2019, 2021; Alemayehu *et al.* 2023).

5.2.3 Anza rift

The slowest wave speeds of Vs ≤ 2.6 km s^{-1} spatially coincide with the Anza rift's depocentre at depths ≤4 km (D–D′ and H–H′, Fig. 9) consistent with depth to crystalline basement as determined by exploratory wells in the rift (e.g. Winn *et al.* 1993) and a surface wave analyses (Kounoudis *et al.* 2023). Additionally, we observe high-velocity anomalies of 3.8–4.0 km s^{-1} at depths of 20–25 km (F–F′ and G–G′, Fig. 9) consistent with Moho depths in this area of $\beta \geq 1.9$ (Kounoudis *et al.* 2023; Ogden *et al.* 2023). The Anza rift basin is overlain by largely un-faulted shield volcanoes and monogenetic cone complexes: some are underlain by low-velocity anomalies. For example, the Holocene Hurri Hills shield complex has relatively low-velocity anomalies of Vs ≤ 3.4 km s^{-1} to depths of ∼ 17 km (LVZ2 in F–F′, Fig. 9).

5.2.4 Oligocene-Recent Lokichar-Kerio rifts

The rift basins west of the Lake Turkana rift formed during a 27–25 Ma pulse of magmatism, but active strain and magmatism are now localized to the Lake Turkana rift (Morley *et al.* 1999; Schofield *et al.* 2021; Muirhead *et al.* 2022; Musila *et al.* 2023). Moho depths constrained by controlled source seismology (KRISP; Mechie *et al.* 1994) in the Lokichar and Kerio rift matches with our 3.8 km/s Moho depth velocity contour (D–D′ and E–E′, Fig. 9).

6 DISCUSSION

The 3-D crustal shear wave velocity (Vs) results from ambient noise tomography provide new constraints on the crustal velocity structure of the Turkana Depression and southernmost Ethiopia. We place our work in the context of the recent TRAILS studies in the region: discrete bulk crustal Vp/Vs and crustal thickness measurements (Ogden *et al.* 2023), surface wave imaging of the crust and uppermost mantle lithosphere (Kounoudis *et al.* 2023), *P*- and *S*-wave body-wave upper-mantle tomography (Kounoudis *et al.* 2021), and active crustal strain zones (Musila *et al.* 2023), as well as earlier 2-D controlled active source imaging (Mechie *et al.* 1994, 1997). Our integrated approach enables us to assess how Neoproterozoic oceanic accreted terranes, Mesozoic-Paleogene failed rift systems, Eocene flood magmatism crustal feeder zones, and Oligo-Miocene-to-Recent faulting and magmatism modify crustal structure.

Episodes of flood magmatism in continental rift systems are relatively short-lived (≤15 My); the efficient way of achieving flood magmatism's rapid outpourings would be through magma chambers feeding dike systems through the crust (e.g. Karlstrom & Richards 2011; Rooney 2017; Mittal *et al.* 2021; Steiner *et al.* 2021).Our new results, when reviewed in light of the geological record, provide context to distinguish between pre-existing compositional variations and frozen Eocene–Oligocene flood basalt plumbing systems, both of which would appear as high-velocity zones.

6.1 Magmatic crustal modification

In southwest Ethiopia, a region that experienced Eocene–Oligocene flood magmatism, has localized (≤50 km-wide) and 10–15 km-thick mid-lower crustal zones of fast Vs anomalies of ≥3.8 km s^{-1} (HVZ1 in A–A′ and B–B′, Fig. 9). This suggests that Eocene–Oligocene flood magmatism was fed by a few widely spaced crustal feeder zones that may have been similar to Marsabit or Hurri Hills. With a crustal thickness of ≥30 km in this region (Ogden *et al.* 2023), the 10–15 km-thick high velocity zones are comparable to the 8–15 km-thick flood magmatism crustal feeder zones observed in the western Ethiopian plateau, north of our study area (e.g. Mackenzie *et al.* 2005) and other continental flood basalt provinces worldwide (e.g. Ridley & Richards 2010). The localized nature of these frozen magma intrusions is also consistent with the absence of elevated Vp/Vs except at stations near eruptive centres (e.g. Weyto basin, Ogden *et al.* 2023) or inferred Eocene–Oligocene magma bodies. Similar patterns of locally high Vs anomalies throughout the crust are observed in other parts of the Ethiopian plateau outside the active rift zones (Alemayehu *et al.* 2023). These locally fast wave speed zones may represent crustal feeder zones for the flood magmatic eruptions (Steiner *et al.* 2021, 2024) (Profile A, Fig. 10).

Oligo-Miocene to Recent syn-rift magmatism, spanning abandoned, active, and incipient rifts, is marked by localized active magma intrusions: active magma intrusions with low Vs (≤ 3.4 km s^{-1}) at depths of 17–20 km (LVZ1 and LVZ2 in C–C′, E–E′ and F–F′, respectively, Fig. 9). For example, the aligned chain of Quaternary eruptive centres in the actively deforming Turkana rift zone is underlain by localized slow velocity zones throughout the crust with pipe-like clusters of earthquakes, suggesting the presence of localized active magma intrusions. The localized nature of these active intrusions differs from the weakly extended central MER to the north whereby the central rift valley is underlain by crustal-scale magma intrusions that underlie aligned chains of Quaternary eruptive centres in the active magmatic rift segments (e.g. Chambers *et al.* 2019, 2022). The isolated Quaternary eruptive centers punctuating the Lake Turkana rift overlie the largest amplitude seismic slow wave speeds at mantle depths of 75 km interpreted as one or a combination of mantle lithosphere thinning and heating with or without a significant melt fraction (Kounoudis *et al.* 2021).

The Quaternary Hurri Hills, located east of the zone of active deformation, are underlain by localized low-velocity anomalies, which also are interpreted as a localized magmatic plumbing system with the underlying mantle lithosphere having 'normal' wave speeds

Downloaded from https://academic.oup.com/gji/article/243/1/ggaf282/8211814 by Imperial College of Science Technology and Medicine user on 12 September 2025

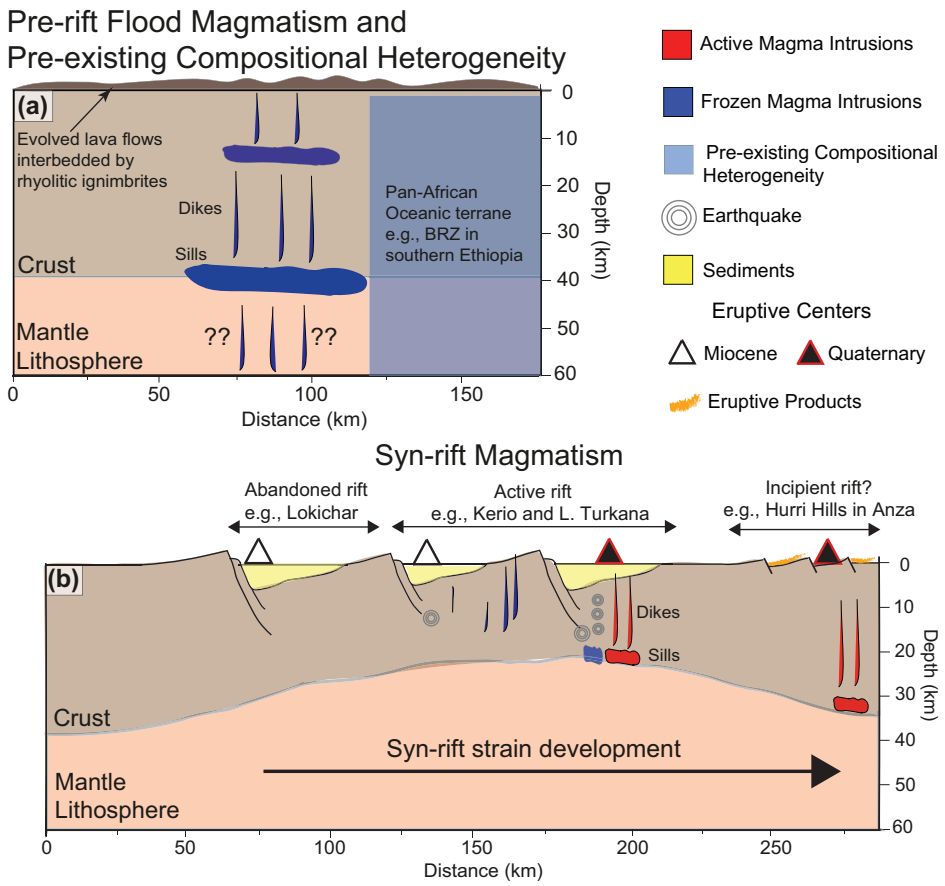


Figure 10. Schematic diagrams summarizing pre-existing compositional heterogeneity, pre-rift flood and syn-rift magmatism synthesized from our Rayleigh Vs models with crustal thickness constrained by existing data. (A) The ≤ 50 km-wide Oligo-Miocene flood magmatism crustal feeder zones with Vs ≥ 3.8 km s^{-1} fed the pre-rift magmatism (e.g. Steiner *et al.* 2021, 2024). Pre-existing compositional heterogeneity associated with the Pan-African oceanic terrane has Vs of ≥ 3.6 km s^{-1} throughout the crust with no surface expression of Miocene-Recent volcanism and no evidence of pre-rift magmatic crustal modification. (B) Oligocene–Miocene to Recent syn-rift strain development. Magmatism is manifested locally as active and/or frozen magma intrusions. BRZ is the broadly rifted zone in southern Ethiopia.

(Kounoudis *et al.* 2023). The Quaternary rift flank volcanoes overlie the slowest sublithospheric mantle wave speeds at depths > 200 km that may source magmas for the region (Kounoudis *et al.* 2021; Boyce *et al.* 2023). These patterns indicate that mantle upwelling(s) as well as lithospheric thinning influence melt production and the distribution of magmatism more than 30 My after initial plume impact (e.g. Kounoudis *et al.* 2021; Cancel-Vazquez *et al.* 2024). The off-rift magma intrusions, in turn, may act as precursors for incipient rifting; heat transfer and metasomatic reactions from the active magma bodies may weaken the plate and facilitate strain migration above the hottest asthenosphere.

6.2 Pre-existing compositional variations

The BRZ in Southern Ethiopia developed in Pan-African oceanic terranes that have high-velocity anomalies throughout the crust (Vs of ≥ 3.6 km s^{-1}, A–A′ and B–B′, Fig. 9) and upper mantle from 50–200 km depth (Kounoudis *et al.* 2021, 2023). This zone has no surface expression of Oligo-Miocene to Recent syn-rift magmatism (e.g. Erbello *et al.* 2024; Sullivan *et al.* 2024). The integrated strength of this cold lithospheric-scale pre-existing mechanical heterogeneity (Fig. S9, Supporting Information) and its relatively low Miocene-Recent crustal stretching factors of ≤1.2 (Fig. 9b; Ogden *et al.* 2023) suggest that this region might have resisted Oligocene–Miocene stretching, contributing to the unusual breadth of the BRZ in southern Ethiopia.

North of the Mesozoic Anza rift's northern border fault, we observe a high-velocity anomaly ≥ 3.8 km s^{-1} up to depths of 15 km (HVZ2 in C–C′ and F–F′, Fig. 9). These high velocity zones corresponds to compositional variations mapped at the surface as a late Precambrian high-grade metamorphic and mafic-ultramafic rocks (Adola belt) accreted during the Pan-African Orogeny (e.g. Worku and Schandelmeier 1996; Yibas *et al.* 2002).

7 CONCLUSIONS

We analysed ambient noise signals continuously recorded between 2019–2021 by the TRAILS seismic network and nearby stations across the 300 km-wide zone of linkage between the Main Ethiopian and Eastern (Kenya) rifts, including the Turkana Depression. We inverted for Rayleigh period maps from 5 to 25 s; the period maps were subsequently inverted for 3-D Rayleigh shear wave velocity (Vs) models. The final 3-D Vs models image the crustal velocity structure of the Turkana Depression and its immediate environs.

Downloaded from https://academic.oup.com/gji/article/243/1/ggaf282/8211814 by Imperial College of Science Technology and Medicine user on 12 September 2025

Our results, integrated with findings from previous seismic and petrological studies, offer insights into the modification of continental crust during flood magmatism. The absence of widespread fast wave speed lower crustal frozen intrusions and active low velocity active intrusions, argues against regional lower crustal intrusions and widespread dike intrusions, consistent with receiver function analyses of Ogden *et al.* (2023). Instead, seismic imaging reveals ≤50 km-wide and 10–15 km-thick localized fast wave speed zones with Vs ≥ 3.8 km s^{-1} at mid-lower crust depths interpreted as crustal feeder zones that fed pre-rift flood magmatism (Fig. 10a; Steiner *et al.* 2021, 2024). Beneath the post-flood basalt phase Lake Turkana rift, Pleistocene-Recent syn-rift eruptive centres are marked by localized zones of low Vs of ≤ 3.4 km s^{-1} at depths of 20 km interpreted as localized active magma intrusions.

The pronounced Miocene-Recent crustal stretching factors of ≥1.9 in the Turkana Depression (Ogden *et al.* 2023) coupled with the lack of widespread magma modification indicate that the thermomechanical modification between ∼27 Ma to as recently as 1–2 Ma was largely achieved through mechanical stretching in this rift sector. During the past 2 Ma, with the localization of strain beneath the Lake Turkana rift, magma-assisted rifting has initiated to connect with the Eastern Rift sector through the Suguta rift (Fig. 10b). The shield volcanoes east of Lake Turkana rift also show crustal-scale low velocity zones indicative of localized active magma intrusions. The transfer of heat and volatiles through the yet unstretched (in the Oligocene-Recent rifting phase) crust may weaken the plate and pre-condition the crust to subsequent extension, in part explaining the west to east migration of rifting in the region.

Pre-existing crustal or lithospheric-scale terranes appear to have played a role in strain localization during early rifting. The NW-trending Pan-African oceanic terranes in southern Ethiopia (e.g. Fritz *et al.* 2013; Verner *et al.* 2021) manifest as high Vs anomalies of 3.6 km s^{-1} throughout the crust; these zones are underlain by high seismic velocity mantle at depths of 50–200 km interpreted as a Proterozoic oceanic accreted terrane (Kounoudis *et al.* 2021, 2023). Owing to the integrated strength of this lithospheric-scale pre-existing mechanical heterogeneity, the mafic Pan-African terrane might have resisted Oligocene–Miocene stretching and magmatism, contributing to the unusual breadth of the BRZ in southern Ethiopia.

ACKNOWLEDGMENTS

We thank editor John Hopper and two anonymous reviewers for constructive feedback that helped us clarify interpretations. CE and MM acknowledge support of the National Science Foundation grant number 1824417 and the Tulane University Vokes Fellowship to MM. Ian Bastow, Chris Ogden and Rita Kounoudis acknowledge support from National Environment Research council grant number NE/S014136/1 and NE/L002515/1. Rita Kounoudis was funded by an Imperial College President's PhD Scholarship. For the purpose of open access, the author has applied a Creative Commons Attribution (CC BY) licence to any Author Accepted Manuscript (AAM) version arising. We acknowledge the following software packages used in our ambient noise study: (1) MsNoise (Lecocq *et al.* (2014); (2) Automatic Frequency Time Analyses (AFTAN; Levshin *et al.* 1972); (3) Senskernel (Levshin *et al.* 1989); (4) Barmin code (Barmin *et al.* 2001); (5) Fatiando (Uieda *et al.* 2013); and (6) Geopsy, Dinver (Wathelet *et al.* 2004, 2005, 2008).

Open Research

SUPPORTING INFORMATION

Supplementary data are available at *GJIRAS* online.

Figure S1. Spatial distribution of the 2019–2021 TRAILS project seismic stations used in our ambient noise tomographic imaging. The inverted triangles are the Ethiopian stations (network 6R, Bastow 2019) whereas the orange triangles are the Kenyan stations (network Y1, Ebinger 2018). GEOFON seismic station LODK is shown as a yellow polygon. Three stations in southern MER, north of Lake Abaya, are part of the Lake Abaya project and are denoted as pink polygons (Ogden *et al.* 2021). Pink polygons indicate two Uppsala Kenya seismic network stations.

Figure S2. [A] ZZ Rayleigh NCF for DILE-NHRK station pair. [B] Fourier transforms of DILE-NHRK NCF. Possible sources of the zero-point noise seen in some of the stacked NCFs include teleseismic *P*-waves generated by distant storms and in deep oceans (Gerstoft *et al.* 2008; Landes et al. 2010) or body waves reflected by the Moho (Zhan *et al.* 2010; Poli *et al.* 2012).

Figure S3. [A] Flipped and stacked positive (causal) and negative (acausal) sides of the noise correlation functions for ZZ Rayleigh DILE-NHRK station pair. [B] Group and phase velocities dispersion curves, obtained by the AFTAN programme (Ritzwoller 2013) for station pairs DILE-NHRK are displayed with the amplitude of signal to noise ratio described in decibels (dB).

Figure S4. All dispersion curves for ZZ Rayleigh waves that passed our dispersion curve selection criteria as described in section 4.2. Lines of minimum and maximum thresholds, displayed as dashed black lines, were selected depending on the distribution of the dispersion curves at all periods. Dispersion curves selected (red) are bounded by 3σ threshold lines, and the grey solid lines are excluded from further analysis. This resulted in 513 accepted and 39 excluded station pairs.

Figure S5. Station-based dispersion curve selection criteria of seismic stations (green triangles) in the Turkana Depression. [A] Accepted (red lines) and excluded (grey lines) dispersion curves for station pairs with station YABE's vertical (ZZ); the dispersion curves are phase velocities. Dispersion curves that are not within standard deviation of 3 from the median (solid blue line) are removed; these are dispersion curves outside the bounding dashed blue lines. [B] Spatial distribution of the accepted dispersion curves in red and excluded in grey. Seismic stations are symbolized in inverted green triangles.

Figure S6. (**A and A′**) Rose diagram plots of the distribution of ZZ Rayleigh and RR Rayleigh dispersion curves that passed our dispersion curve selection criteria and whose length are scaled by their SNR. (**A′** and **B′**) SNR heat map of the dispersion curves at each channel. The inverted black triangles are seismic stations used in this study.

Figure SM7. ZZ Rayleigh trade-off curve that plots model RMS against regularization parameters. If we chose the set of regularization parameters suggested by Barmin *et al.* (2001), based on our 0.2° nodal separation, we obtain Model Q that has relatively high model roughness with lower model residual. We select the set of regularization parameters that matches with the model at the inflection point of our trade-off curve, Model I∗.

Figure S8. 1-D shear wave velocity models at different locations in the Turkana Depression from our ZZ Rayleigh phase velocities. [A], [B] and [C] are ZZ Rayleigh waves 1-D velocity models sampling the broadly rifted zone, Mesozoic-Paleogene Anza rift and Oligo-Miocene to Recent Omo-Turkana rift, respectively. The blue–green–yellow–red are the accepted models that have have ≤10

Downloaded from https://academic.oup.com/gji/article/243/1/ggaf282/8211814 by Imperial College of Science Technology and Medicine user on 12 September 2025

per cent misfit from the extracted depth dispersion curves at each node whereas the gray models below the misfit threshold. The white solid line is the weighted mean for all blue–green–yellow–red accepted models used at each grid to form the final 3-D Vs models.

Figure S9. Yield Strength Envelope simulations illustrating plate strength variations across different regions of the Turkana Depression and its immediate environs. (A) Crustal thickness for both 'normal' and oceanic 'accreted terrane' is 38 km (Ogden *et al.* 2023). Byerlee's law for the hydrated brittle 'normal' granitic upper crust and oceanic 'accreted terrane' upper crust (e.g. Fritz *et al.* 2013) is based on Burgmann & Dresen (2008). Ductile creep hydrated mafic granulitic lower 'normal' and 'terrane' crust is after Wang *et al.* (2012). Depths for 'normal' and 'accreted terrane' LAB are 80 and 100 km, respectively with adiabats of 1450 °C (Kounoudis *et al.* 2023, 2024). In both mantle lithospheric domains, we modelled for a hydrated mantle Peridotite rock following Goetze & Evans (1979). (B) Crustal thickness for 'normal' is 38 km whereas for the failed 'Anza' rift is 25 km (Ogden *et al.* 2023). In both upper crustal domains, we modelled using Byerlee's law for the hydrated brittle 'normal' granitic upper crust. We modelled for a ductile creep hydrated mafic granulitic lower 'normal' and 'Anza' crust is after Wang *et al.* (2012). Depths for 'normal' and 'Anza' LAB depths are 80 km with adiabats of 1450 and 1400 °C, respectively (Kounoudis *et al.* 2023, 2024). 'Normal' mantle lithosphere was modelled using a hydrated mantle Peridotite rock whereas for the failed 'Anza' rift, we modelled for a dry and dehydrated mantle lithosphere (Kounoudis *et al.* 2023). In panels (A) and (B), we assumed a uniform conductive geothermal gradient consistent with lithospheric thickness and adiabat temperature variations. Fossilized pre-existing plate-scale structures such as Neoproterozoic 'accreted terranes' in southern Ethiopian (A) and the failed Mesozoic 'Anza' rift (B) are stronger than 'normal' lithosphere based on their modelled effective elastic thickness variations relative to 'normal' lithosphere west of Lake Turkana where EAR rift initiated in this region.

Table S1. Parameters used to invert for ZZ Rayleigh wave shear wave models using the neighbourhood inversion algorithm, Dinver inversion (Sambridge 1999; Wathelet *et al.* 2004, 2005, 2008). There is parametrization layer overlap to ensure that the inversion is guided by both the *a priori* information and the observational data, the depth integrated dispersion curves.

Please note: Oxford University Press is not responsible for the content or functionality of any supporting materials supplied by the authors. Any queries (other than missing material) should be directed to the corresponding author for the paper.

DATA AVAILABILITY

Seismic data obtained from the TRAILS project and used in this study are archived at IRIS under network codes Y1 (Ebinger 2018) and 6R (Bastow, 2019). Data from an additional permanent seismic station, LODK, was sourced from GEON data centre (GEOFON 1993). Further north in the study area, in southern MER, we used seismic data from network 1Q, also archived at IRIS (Bastow, I., Keir, D., Ayele, A., Ogden, C., Birhanu Abera & Sisay Alemayehu Angere (2019). Northern Lake Abaya Broadband Network [Dataset]. International Federation of Digital Seismograph Networks. https://doi.org/10.7914/SN/1Q_2019). Derived products are available by request.

REFERENCES

Afonso, J.C. *et al.*, 2022. Thermochemical structure and evolution of cratonic lithosphere in central and southern Africa, *Nat. Geosci.,* **15,** 405–410

Alemayehu, S. *et al.*, 2023. Structure of the crust-uppermost mantle beneath the Ethiopian volcanic province using ambient seismic noise and teleseismic *P*-wave coda autocorrelation, *Tectonophysics,* **869,** 230 092.

Barmin, M.P., Ritzwoller, M.H. & Levshin, A.L., 2001. A fast and reliable method for surface wave tomography, in *Monitoring the Comprehensive Nuclear-Test-Ban Treaty: Surface Waves,* pp. 1351–1375, eds, Levshin, A.L. & Ritzwoller, M.H., Birkhäuser.

Bastow, I., 2019. Turkana Rift arrays to investigate lithospheric strains—UK component, *International Federation of Digital Seismograph Networks*.

Bastow, I., Keir, D., Ayele, A., Ogden, C., Abera, B. & Angere, S.A., 2019. Northern Lake Abaya Broadband Network . International Federation of Digital Seismograph Networks, .

Benoit, M.H., Nyblade, A.A. & Pasyanos, M.E., 2006. Crustal thinning between the Ethiopian and East African plateaus from modeling Rayleigh wave dispersion, *Geophys. Res. Lett.,* **33**.

Bensen, G.D., Ritzwoller, M.H., Barmin, M.P., Levshin, A.L., Lin, F., Moschetti, M.P., Shapiro, N.M. & Yang, Y., 2007. Processing seismic ambient noise data to obtain reliable broad-band surface wave dispersion measurements, *Geophys. J. Int.,* **169,** 1239–1260.

Bosworth, W. & Morley, C.K., 1994. Structural and stratigraphic evolution of the Anza rift, Kenya, *Tectonophysics,* **236,** 93–115.

Boyce, A., Kounoudis, R., Bastow, I.D., Cottaar, S., Ebinger, C.J. & Ogden, C.S., 2023. Mantle wavespeed and discontinuity structure below East Africa: implications for cenozoic hotspot tectonism and the development of the Turkana Depression, *Geochem. Geophys. Geosyst.,* **24,** e2022GC010775.

Brenguier, F., Shapiro, N.M., Campillo, M., Nercessian, A. & Ferrazzini, V., 2007. 3-D surface wave tomography of the Piton de la Fournaise volcano using seismic noise correlations, *Geophys. Res. Lett.,* **34**.

Brocher, T.M., 2005. Empirical relations between elastic wavespeeds and density in the earth's crust, *Bull. Seism. Soc. Am.,* **95,** 2081–2092.

Brune, S., Corti, G. & Ranalli, G., 2017. Controls of inherited lithospheric heterogeneity on rift linkage: numerical and analog models of interaction between the Kenyan and Ethiopian rifts across the Turkana depression, *Tectonics,* **36,** 1767–1786.

Brune, S., Kolawole, F., Olive, J.-A., Stamps, D.S., Buck, W.R., Buiter, S.J.H., Furman, T. & Shillington,, D.J., 2023. Geodynamics of continental rift initiation and evolution, *Nat. Rev. Earth Environ.,* **4,** 235–253.

Bürgmann, R. & Dresen, G., 2008. Rheology of the lower crust and upper mantle: evidence from rock mechanics, geodesy, and field observations, *Annu. Rev. Earth Planet. Sci.,* **36,** 531–567.

Cancel Vazquez, S.M., Rooney, T.O., Brown, E.L., Bollinger, A., Bastow, I.D., Steiner, R.A. & Kappelman, J., 2024. Basaltic pulses and lithospheric thinning—Plio-pleistocene magmatism and rifting in the Turkana Depression (East African Rift System), *J. Geophys. Res. Solid Earth,* **129,** e2024JB029166.

Chambers, E.L., Harmon, N., Keir, D. & Rychert, C.A., 2019. Using ambient noise to image the Northern East African Rift, *Geochem. Geophys. Geosyst.,* **20,** 2091–2109.

Chambers, E.L., Harmon, N., Rychert, C.A. & Keir, D., 2021. Variations in melt emplacement beneath the northern East African Rift from radial anisotropy, *Earth planet. Sci. Lett.,* **573,** 117 150.

Chambers, Emma L., Harmon, Nicholas., Rychert, Catherine A., Gallacher, Ryan J. & Keir, Derek., 2022. Imaging the seismic velocity structure of the crust and upper mantle in the northern East African Rift using Rayleigh wave tomography, *Geophysical Journal International,* **230** (3), 2036.

Chin, E.J., 2018. Deep crustal cumulates reflect patterns of continental rift volcanism beneath Tanzania, *Contrib. Mineral. Petrol.,* **173,** 85.

Civilini, F., Mooney, W.D., Savage, M.K. & Townend, J., 2023. Ambient seismic noise tomography of the Kingdom of Saudi Arabia (No. 1862-N), *Professional Paper*, U.S. Geological Survey.

Civilini, F., Mooney, W.D., Savage, M.K., Townend, J. & Zahran, H., 2019. Crustal imaging of northern Harrat Rahat, Saudi Arabia, from ambient noise tomography, *Geophys. J. Int.,* **219,** 1532–1549.

Downloaded from https://academic.oup.com/gji/article/243/1/ggaf282/8211814 by Imperial College of Science Technology and Medicine user on 12 September 2025

Cornwell, D.G., Mackenzie, G.D., England, R.W., Maguire, P.K.H., Asfaw, L.M. & Oluma, B., 2006. Northern Main Ethiopian Rift crustal structure from new high-precision gravity data, in *The Afar Volcanic Province within the East African Rift System,* Vol., **259,** pp. 0, eds, Yirgu, G., Ebinger, C.J. & Maguire, P.K.H., Geological Society of London.

Corti, G. *et al.*, 2019. Aborted propagation of the Ethiopian rift caused by linkage with the Kenyan rift, *Nat. Commun.,* **10,** 1309.

Davidson, A. & Rex, D.C., 1980. Age of volcanism and rifting in southwestern Ethiopia, *Nature,* **283,** 657–658.

Dindi, E.W., 1994. Crustal structure of the Anza graben from gravity and magnetic investigations, *Tectonophysics,* **236,** 359–371.

Dodson, R.G., 1963. Geology of the South Horr area, *Rep. Geol. Surv. Kenya,* **60,** 1–53.

Dugda, M.T., Nyblade, A.A., Julia, J., Langston, C.A., Ammon, C.J. & Simiyu, S., 2005. Crustal structure in Ethiopia and Kenya from receiver function analysis: implications for rift development in eastern Africa, *J. Geophys. Res. Solid Earth,* **110,**

Dunkelman, T.J., Rosendahl, B.R. & Karson, J.A., 1989. Structure and stratigraphy of the Turkana rift from seismic reflection data, *J. Afr. Earth Sci. (and the Middle East),* **8,** 489–510.

Ebinger, C.J. & Ibrahim, A., 1994. Multiple episodes of rifting in Central and East Africa: a re-evaluation of gravity data, *Geol. Rundsch.,* **83,** 689–702.

Ebinger, C.J., 2018. *Crust and Mantle Structure and the Expression of Extension in the Turkana Depression of Kenya and Ethiopia*. International Federation of Digital Seismograph Networks.

Ebinger, C.J., 2021. *Recipe for Rifting: Flavors of East Africa,* Elsevier.

Ebinger, C.J., Yemane, T., Harding, D.J., Tesfaye, S., Kelley, S. & Rex, D.C., 2000. Rift deflection, migration, and propagation: linkage of the Ethiopian and Eastern rifts, Africa, *Geol. Soc. Am. Bull.,* **112,** 163–176.

Ebinger, C.J., Yemane, T., Woldegabriel, G., Aronson, J.L. & Walter, R.C., 1993. Late Eocene–Recent volcanism and faulting in the southern main Ethiopian rift, *JGS,* **150,** 99–108.

Emry, E.L., Shen, Y., Nyblade, A.A., Flinders, A. & Bao, X., 2019. Upper mantle earth structure in Africa from full-wave ambient noise tomography, *Geochem. Geophys. Geosyst.,* **20,** 120–147.

Erbello, A.., Colleps, C.., Melnick, D.., Sobel, E. R.., Bookhagen, B.., Pingel, H.., Zeilinger, G.., van der Beek, P. & Strecker, M. R.., 2024. Magma-Assisted Continental Rifting: The Broadly Rifted Zone in SW Ethiopia, East Africa, *Tectonics,* **43** (1).

French, S.W. & Romanowicz, B., 2015. Broad plumes rooted at the base of the Earth's mantle beneath major hotspots, *Nature,* **525,** 95–99.

Fritz, H., Abdelsalam, M., Ali, K.A., Bingen, B., Collins, A.S., Fowler, A.R., Ghebreab, W. *et al.*, 2013. Orogen styles in the East African Orogen: a review of the neoproterozoic to cambrian tectonic evolution, *J. Afr. Earth Sci.,* **86,** 65–106.

Furman, T., Nelson, W.R. & Elkins-Tanton, L.T., 2016. Evolution of the East African rift: drip magmatism, lithospheric thinning and mafic volcanism, *Geochim. Cosmochim. Acta,* **185,** 418–434.

GEOFON Data Centre, 1993. GEOFON Seismic Network, GFZ Data Services,

George, R., Rogers, N. & Kelley, S., 1998. Earliest magmatism in Ethiopia: evidence for two mantle plumes in one flood basalt province, *Geology,* **26,** 923–926.

Gerstoft, P., Shearer, P.M., Harmon, N. & Zhang, J., 2008. Global P, PP, and PKP wave microseisms observed from distant storms, *Geophys. Res. Lett.,* **35,** 2008GL036111.

Goetze, C. & Evans, B., 1979. Stress and temperature in the bending lithosphere as constrained by experimental rock mechanics, *Geophys. J. Int.,* **59,** 463–478.

Guerri, M., Cammarano, F. & Connolly, J.A.D., 2015. Effects of chemical composition, water and temperature on physical properties of continental crust, *Geochem. Geophys. Geosyst.,* **16,** 2431–2449.

Guth, A.L., 2016. Volcanic volumes associated with the Kenya Rift: recognition and correction of preservation biases, Retrieved fromhttps://pubs.geoscienceworld.org/books/edited-volume/1515/chapter/107190544(accessed 23 July 2024).

Hendrie, D.B., Kusznir, N.J., Morley, C.K. & Ebinger, C.J., 1994. Cenozoic extension in northern Kenya: a quantitative model of rift basin development in the Turkana region, *Tectonophysics,* **236,** 409–438.

Karlstrom, L. & Richards, M., 2011. On the evolution of large ultramafic magma chambers and timescales for flood basalt eruptions, *J. Geophys. Res.,* **116,** B08216.

Kebede, B., Mammo, T., Shawel, M. & Alemu, T., 2023. Integrated seismic stratigraphic and structural analysis of Southern main Ethiopian rift basin: implications for hydrocarbon potentials, *Acta Geophys.,* **72,** 597–617.

Kim, S., Nyblade, A.A., Rhie, J., Baag, C.-E. & Kang, T.-S., 2012. Crustal *S*-wave velocity structure of the Main Ethiopian Rift from ambient noise tomography, *Geophys. J. Int.,* **191,** 865–878.

Knappe, E. *et al.*, 2020. Accommodation of East African rifting across the Turkana depression, *JGR Solid Earth,* **125,** e2019JB018469.

Kounoudis, R. *et al.*, 2021. Body-wave tomographic imaging of the Turkana depression: implications for rift development and plume-lithosphere interactions, *Geochem. Geophys. Geosyst.,* **22,** e2021GC009782.

Kounoudis, R. *et al.*, 2023. The development of rifting and magmatism in the multiply rifted Turkana Depression, East Africa: evidence from surface-wave analysis of crustal and uppermost mantle structure, *Earth planet. Sci. Lett.,* **621,** 118 386.

Kounoudis, R., Bastow, I.D., Ebinger, C.J., Zhou, P., Goes, S.D., Musila, M., Ogden, C.S.S. & Ayele, A., 2024. Variable magmatic modification of the East African lithosphere, AGU Fall Meeting 2024, Washington, D.C.

Landès, M., Hubans, F., Shapiro, N.M., Paul, A. & Campillo, M., 2010. Origin of deep ocean microseisms by using teleseismic body waves, *J. geophys. Res.,* **115,** 2009JB006918.

Lecocq, T., Caudron, C. & Brenguier, F., 2014. MSNoise, a python package for monitoring seismic velocity changes using ambient seismic noise, *Seismol. Res. Lett.,* **85,** 715–726.

Levshin, A.L., Pisarenko, V.F. & Pogrebinsky, G.A., 1972. On a frequency-time analysis of oscillations, *Annales de Geophysique,* **28,** 211–218.

Levshin, A.L., Yanovskaya, T.B., Lander, A.V., Bukchin, B.G., Barmin, M.P., Ratnikova, L.I. & Its, E.N., 1989. *Seismic Surface Waves in a Laterally Inhomogeneous Earth,* Kluwer Academic Publishers.

Lin, F.-C., Moschetti, M.P. & Ritzwoller, M.H., 2008. Surface wave tomography of the western United States from ambient seismic noise: rayleigh and Love wave phase velocity maps, *Geophys. J. Int.,* **173,** 281–298.

Mackenzie, G.D., Thybo, H. & Maguire, P.K.H., 2005. Crustal velocity structure across the Main Ethiopian Rift: results from two-dimensional wide-angle seismic modelling, *Geophys. J. Int.,* **162,** 994–1006.

Maguire, P.K.H. *et al.*, 2006. Crustal structure of the northern Main Ethiopian Rift from the EAGLE controlled-source survey; a snapshot of incipient lithospheric break-up, Retrieved fromhttps://pubs.geoscienceworld.org/books/edited-volume/1915/chapter/107433188 (accessed 7 August 2024).

Mechie, J., Keller, G.R., Prodehl, C., Gaciri, S., Braile, L.W., Mooney, W.D., Gajewski, D. & Samdmeier, K.-J., 1994. Crustal structure beneath the Kenya Rift from axial profile data, *Tectonophysics,* **236,** 179–200.

Mechie, J., Keller, G.R., Prodehl, C., Khan, M.A. & Gaciri, S.J., 1997. A model for the structure, composition and evolution of the Kenya rift, *Tectonophysics,* **278,** 95–119.

Mittal, T. & Richards, M.A., 2021. The magmatic architecture of continental flood basalts: 2. A new conceptual model, *JGR Solid Earth,* **126,** e2021JB021807.

Mittal, T., Richards, M.A. & Fendley, I.M., 2021. The magmatic architecture of continental flood basalts I: observations from the deccan traps, *JGR Solid Earth,* **126,** e2021JB021808.

Morley, C.K., 2020. Early syn-rift igneous dike patterns, northern Kenya Rift (Turkana, Kenya): implications for local and regional stresses, tectonics, and magma-structure interactions, *Geosphere,* **16,** 890–918.

Morley, C.K., Karanja, F.M., Wescott, W.A., Stone, D.M., Harper, R.M., Wigger, S.T. & Day, R.A., 1999. Geology and geophysics of the western Turkana basins, Kenya, Retrieved fromhttps://pubs.geoscienceworld.org/aapg/books/edited-volume/1299/chapter-abstract/107165294 (accessed 14 June 2024).

Downloaded from https://academic.oup.com/gji/article/243/1/ggaf282/8211814 by Imperial College of Science Technology and Medicine user on 12 September 2025

Morley, C.K., Wescott, W.A., Stone, D.M., Harper, R.M., Wigger, S.T. & Karanja, F.M., 1992. Tectonic evolution of the northern Kenyan Rift, *JGS,* **149,** 333–348.

Mosley, P.N., 1993. Geological evolution of the late proterozoic "Mozambique Belt" of Kenya, *Tectonophysics,* **221,** 223–250.

Muirhead, J.D., Scholz, C.A. & O. Rooney, T., 2022. Transition to magma-driven rifting in the South Turkana Basin, Kenya: part 1, *JGS,* **179,** jgs2021–159.

Musila, M. *et al.*, 2023. Active deformation constraints on the Nubia-Somalia plate boundary through heterogenous lithosphere of the Turkana depression, *Geochem. Geophys. Geosyst.,* **24,** e2023GC010982.

Neves, S.P., Tommasi, A., Vauchez, A. & Carrino, T.A., 2021. The Borborema strike-slip shear zone system (NE Brazil): large-scale intracontinental strain localization in a heterogeneous plate, *Lithosphere,* **2021,** 6407 232.

Nutz, A., Ragon, T. & Schuster, M., 2022. Cenozoic tectono-sedimentary evolution of the northern Turkana Depression (East African Rift System) and its significance for continental rifts, *Earth planet. Sci. Lett.,* **578,** 117 285.

Nyblade, Andrew A.., 2011. *Volcanism and Evolution of the African Lithosphere,* .

Ogden, C.S. *et al.*, 2021. Seismicity and crustal structure of the Southern Main Ethiopian Rift: new evidence from Lake Abaya, *Geochem. Geophys. Geosyst.,* **22,** e2021GC009831.

Ogden, C.S. *et al.*, 2023. The development of multiple phases of superposed rifting in the Turkana Depression, East Africa: evidence from receiver functions, *Earth Planet. Sci. Lett.,* **609,** 118 088.

Özaydın, S., Selway, K., Foley, S.F., Ezad, I.S., Griffin, W.L., Tarits, P.S. & Hautot, S., 2024. Role of metasomatism in the development of the East African Rift at the Northern Tanzanian divergence: insights from 3D magnetotelluric modeling, *Geochem. Geophys. Geosyst.,* **25,** e2023GC011191.

Poli, P., Pedersen, H.A. & Campillo, M., 2012. Emergence of body waves from cross-correlation of short period seismic noise, *Geophys. J. Int.,* **188,** 549–558.

Prodehl, C., Jacob, A.W.B., Thybo, H., Dindi, E. & Stangl, R., 1994. Crustal structure on the northeastern flank of the Kenya rift, *Tectonophysics,* **236,** 271–290.

Pusok, Adina E.., Li, Yuan., Davis, Tim., May, Dave A.. & Katz, Richard F.., 2025. Inefficient Melt Transport Across a Weakened Lithosphere Led to Anomalous Rift Architecture in the Turkana Depression, *Geophysical Research Letters,* **52** (11).

Ragon, Théa., Nutz, Alexis., Schuster, Mathieu., Ghienne, Jean-Francois., Ruffet, Gilles., Rubino, Jean-Loup. & Patacci, M.., 2018. Evolution of the northern Turkana Depression (East African Rift System, Kenya) during the Cenozoic rifting: New insights from the Ekitale Basin (28-25.5 Ma), *Geological Journal,* **54** (6), 3468.

Ridley, V.A. & Richards, M.A., 2010. Deep crustal structure beneath large igneous provinces and the petrologic evolution of flood basalts, *Geochem. Geophys. Geosyst.,* **11,** 2009GC002935.

Ritsema, J., Deuss, A., Van Heijst, H.J. & Woodhouse, J.H., 2011. S40RTS: a degree-40 shear-velocity model for the mantle from new Rayleigh wave dispersion, teleseismic traveltime and normal-mode splitting function measurements, *Geophys. J. Int.,* **184,** 1223–1236.

Ritzwoller, M.H.(2013) AFTAN [automatic frequency-time analysis] of ambient noise cross-correlations. *University of Colorado Boulder software release*. Available at:http://ciei.colorado.edu/Products/ (accessed 3 February 2023)

Rooney, T.O., 2017. The cenozoic magmatism of East-Africa: part I—Flood basalts and pulsed magmatism, *Lithos,* **286,** 264–301.

Sambridge, M., 1999. Geophysical inversion with a neighbourhood algorithm—I. Searching a parameter space, *Geophys. J. Int.,* **138,** 479–494.

Schofield, N., Newton, R., Thackrey, S., Watson, D., Jolley, D. & Morley, C., 2021. Linking surface and subsurface volcanic stratigraphy in the Turkana Depression of the East African Rift system, *J. Geol. Soc.,* **178,** jgs2020–110

Shackleton, R.M., 1986. Precambrian collision tectonics in Africa, *Geol. Soc. London Spec. Publ.,* **19,** 329–349.

Shapiro, N.M., Campillo, M., Stehly, L. & Ritzwoller, M.H., 2005. High-resolution surface-wave tomography from ambient seismic noise, *Science,* **307,** 1615–1618.

Snieder, R., 2004. Classical physics, including nonlinear media and photonic materials-extracting the Green's function from the correlation of coda waves: a derivation based on stationary phase, *Phys. Rev.-Section E-Statistical Nonlinear and Soft Matter Physics,* **69**(4), 46610–46610.

Steiner, R Alex., Rooney, Tyrone O., Kappelman, John., Lydic, Todd., Girard, Guillaume., Mariita, Nicholas. & Phillips, Rayn., 2024. Messengers from the Magma Chambers: Petrostratigraphic Analysis of Plagioclase-Rich Flood Basalt Lavas in Turkana, Kenya, *Journal of Petrology,* **65** (6).

Steiner, R. Alex., Rooney, Tyrone O.., Girard, Guillaume., Rogers, Nick., Ebinger, Cynthia J.., Peterson, Liam. & Phillips, Rayn K.., 2021. Initial Cenozoic magmatic activity in East Africa: new geochemical constraints on magma distribution within the Eocene continental flood basalt province, *Geological Society, London, Special Publications,* **518** (1), 435.

Stern, R.J., Ali, K.A., Abdelsalam, M.G., Wilde, S.A. & Zhou, Q., 2012. U–Pb zircon geochronology of the eastern part of the Southern Ethiopian Shield, *Precambrian Res.,* **206,** 159–167 Elsevier.

Stuart, G.W.., Bastow, I.D.. & Ebinger, C.J.., 2006. Crustal structure of the northern Main Ethiopian Rift from receiver function studies, *Geological Society, London, Special Publications,* **259** (1), 253.

Sullivan, G., Ebinger, C.J., Musila, M., Perry, M., Kraus, E.R., Bastow, I. & Bendick, B., 2024. Kinematics of rift linkage between the Eastern and Ethiopian rifts in the Turkana Depression, Africa, *Basin Res.,* **36,** e12900.

Teklay, M., Kröner, A., Mezger, K. & Oberhänsli, R., 1998. Geochemistry, Pb□ Pb single zircon ages and Nd□ Sr isotope composition of precambrian rocks from southern and eastern Ethiopia: implications for crustal evolution in East Africa, *J. Afr. Earth Sci.,* **26,** 207–227.

Torres Acosta, V., Bande, A., Sobel, E.R., Parra, M., Schildgen, T.F., Stuart, F. & Strecker, M.R., 2015. Cenozoic extension in the Kenya Rift from low-temperature thermochronology: links to diachronous spatiotemporal evolution of rifting in East Africa, *Tectonics,* **34,** 2367–2386.

Uieda, L., Oliveira, V.C., Jr & Barbosa, V.C., 2013. Modeling the Earth with Fatiando a Terra, *SciPy,* 92pp., Retrieved fromhttps://www.academia.edu/download/98372702/uieda.pdf(accessed 17 October 2023).

Verner, K. *et al.*, 2021. Tectonometamorphic evolution and U–Pb dating of the high-grade Hammar Domain (Southern Ethiopian Shield); implications for the East-African Orogeny, *Precambrian Res.,* **361,** 106 270.

Wang, Y.F., Zhang, J.F., Jin, Z.M. & Green Ii, H.W., 2012. Mafic granulite rheology: implications for a weak continental lower crust, *Earth Planet. Sci. Lett.,* **353,** 99–107.

Wathelet, M., 2005. Array recordings of ambient vibrations: surface-wave inversion, PhD thesis.

Wathelet, M., 2008. An improved neighborhood algorithm: parameter conditions and dynamic scaling, *Geophys. Res. Lett.,* **35,** 2008GL033256.

Wathelet, M., Jongmans, D. & Ohrnberger, M., 2004. Surface-wave inversion using a direct search algorithm and its application to ambient vibration measurements, *Near Surf. Geophys.,* **2,** 211–221.

Wenker, S. & Beaumont, C., 2018. Effects of lateral strength contrasts and inherited heterogeneities on necking and rifting of continents, *Tectonophysics,* **746,** 46–63.

Wescott, W.A., Wigger, S.T., Stone, D.M. & Morley, C.K., 1999. Geology and geophysics of the Lotikipi Plain, Retrieved from https://pubs.geoscienceworld.org/aapg/books/edited-volume/1299/chapter-abstract/107165296(accessed 7 July 2024)

Westerhof, A.B. *et al.*, 2014. Geology and Geodynamic Development of Uganda with Explanation of the 1: 1,000,000 Scale Geological Map, Geological Survey of Finland.

Winn, R.D., Jr, Steinmetz, J.C. & Kerekgyarto, W.L., 1993. Stratigraphy and rifting history of the mesozoic-cenozoic Anza rift, Kenya, *AAPG Bull.,* **77,** 1989–2005.

Downloaded from https://academic.oup.com/gji/article/243/1/ggaf282/8211814 by Imperial College of Science Technology and Medicine user on 12 September 2025

Worku, H. & Schandelmeier, H., 1996. Tectonic evolution of the neoproterozoic Adola Belt of southern Ethiopia: evidence for a Wilson Cycle process and implications for oblique plate collision, *Precambrian Res.,* **77,** 179–210.

Yibas, B., Reimold, W.U., Armstrong, R., Koeberl, C., Anhaeusser, C.R. & Phillips, D., 2002. The tectonostratigraphy, granitoid geochronology and geological evolution of the Precambrian of southern Ethiopia, *J. Afr. Earth Sci.,* **34,** 57–84.

Zhan, Z., Ni, S., Helmberger, D.V. & Clayton, R.W., 2010. Retrieval of Moho-reflected shear wave arrivals from ambient seismic noise, *Geophys. J. Int.,* **182,** 408–420.

Downloaded from https://academic.oup.com/gji/article/243/1/ggaf282/8211814 by Imperial College of Science Technology and Medicine user on 12 September 2025

© The Author(s) 2025. Published by Oxford University Press on behalf of The Royal Astronomical Society. This is an Open Access article distributed under the terms of the Creative Commons Attribution License (https://creativecommons.org/licenses/by/4.0/), which permits unrestricted reuse, distribution, and reproduction in any medium, provided the original work is properly cited.